Microdamage Healing in Asphalt and Asphalt Concrete, Volume III: A Micromechanics Fracture and Healing Model for Asphalt Concrete

PUBLICATION NO. FHWA-RD-98-143

JUNE 2001

U.S. Department of Transportation
Federal Highway Administration

Research, Development, and Technology
Turner-Fairbank Highway Research Center
6300 Georgetown Pike
McLean, VA 22101-2296

Technical Report Documentation Page

1. Report No.	2. Government Accession No.	3. Recipient's Catalog No.
FHWA-RD-98-143		

4. Title and Subtitle	5. Report Date
Microdamage Healing in Asphalt and Asphalt Concrete, Volume III: AmMicromechanics Fracture and Healing Model for Asphalt Concrete	June 2001
	6. Performing Organization Code

7. Author(s)	8. Performing Organization Report No.
R. L. Lytton, C. W. Chen and Dallas N. Little	Research Report 7229

9. Performing Organization Name and Address	10. Work Unit No. (TRAIS)
Texas Transportation Institute The Texas A&M University System College Station, Texas 77843-3135	11. Contract or Grant No. DTFH61-92-C-00170

12. Sponsoring Agency Name and Address	13. Type of Report and Period Covered
Western Research Institute (WRI) P.O. Box 3395 University Station Laramie, Wyoming 82071	Final: February 1998
	14. Sponsoring Agency Code

15. Supplementary Notes

Research performed in cooperation with the Federal Highway Administration.
Research Project Title: Fundamental Properties of Asphalts and Modified Asphalts
Task K - Microdamage Healing in Asphalt and Asphalt Concrete

16. Abstract

Volume 3 documents the development of a micromechanics fracture and healing model for asphalt concrete. This model can be used to calculate the density and growth of microcracks during repeated direct tensile controlled-strain loading. The model is based on a relationship among stiffness changes in the mixture as damage occurs, the rate of change in dissipated pseudo strain energy as loading are applied to the samples and as damage occurs and mixture properties including crack length changes upon loading and mixture cohesive surface energies. The report demonstrates that microcrack growth is the dominate mode of distress at temperatures below 25C and that microcrack healing is the dominate mode of recovery of dissipated pseudo strain energy at these test temperatures. However, at temperatures above about 25C, the predominate mode of distress is plastic damage. Cracking rates during fatigue damage are related to de-wetting cohesive surface energy measurements of the bitumen whereas microcracking healing rates are related to wetting cohesive surface energy measurements of the bitumen. Surface energies of five bitumens with widely different chemical compositions were found to correlate strongly with healing properties as defined by viscoelastic fracture and healing theory.

17. Key Words	18. Distribution Statement
viscoelastic fracture, fatigue damage, tensile fatigue, pseudo-strain	No restrictions. This document is available to the public through NTIS: National Technical Information Service 5285 Port Royal Road Springfield, Virginia 22161

19. Security Classif.(of this report)	20. Security Classif.(of this page)	21. No. of Pages	22. Price
Unclassified	Unclassified	78	

SI* (MODERN METRIC) CONVERSION FACTORS

APPROXIMATE CONVERSIONS TO SI UNITS

Symbol	When You Know	Multiply By	To Find	Symbol
	LENGTH			
in	inches	25.4	millimeters	mm
ft	feet	0.305	meters	m
yd	yards	0.914	meters	m
mi	miles	1.61	kilometers	km
	AREA			
in^2	square inches	645.2	square millimeters	mm^2
ft^2	square feet	0.093	square meters	m^2
yd^2	square yards	0.836	square meters	m^2
ac	acres	0.405	hectares	ha
mi^2	square miles	2.59	square kilometers	km^2
	VOLUME			
fl oz	fluid ounces	29.57	milliliters	mL
gal	gallons	3.785	liters	L
ft^3	cubic feet	0.028	cubic meters	m^3
yd^3	cubic yards	0.765	cubic meters	m^3
NOTE: Volumes greater than 1000 l shall be shown in m^3.				
	MASS			
oz	ounces	28.35	grams	g
lb	pounds	0.454	kilograms	kg
T	short tons (2000 lb)	0.907	megagrams (or "metric ton")	Mg (or "t")
	TEMPERATURE (exact)			
°F	Fahrenheit temperature	5(F-32)/9 or (F-32)/1.8	Celcius temperature	°C
	ILLUMINATION			
fc	foot-candles	10.76	lux	lx
fl	foot-Lamberts	3.426	candela/m^2	cd/m^2
	FORCE and PRESSURE or STRESS			
lbf	poundforce	4.45	newtons	N
lbf/in^2	poundforce per square inch	6.89	kilopascals	kPa

APPROXIMATE CONVERSIONS FROM SI UNITS

Symbol	When You Know	Multiply By	To Find	Symbol
	LENGTH			
mm	millimeters	0.039	inches	in
m	meters	3.28	feet	ft
m	meters	1.09	yards	yd
km	kilometers	0.621	miles	mi
	AREA			
mm^2	square millimeters	0.0016	square inches	in^2
m^2	square meters	10.764	square feet	ft^2
m^2	square meters	1.195	square yards	yd^2
ha	hectares	2.47	acres	ac
km^2	square kilometers	0.386	square miles	mi^2
	VOLUME			
mL	milliliters	0.034	fluid ounces	fl oz
L	liters	0.264	gallons	gal
m^3	cubic meters	35.71	cubic feet	ft^3
m^3	cubic meters	1.307	cubic yards	yd^3
	MASS			
g	grams	0.035	ounces	oz
kg	kilograms	2.202	pounds	lb
Mg (or "t")	megagrams (or "metric ton")	1.103	short tons (2000 lb)	T
	TEMPERATURE (exact)			
°C	Celcius temperature	1.8C + 32	Fahrenheit temperature	°F
	ILLUMINATION			
lx	lux	0.0929	foot-candles	fc
cd/m^2	candela/m^2	0.2919	foot-Lamberts	fl
	FORCE and PRESSURE or STRESS			
N	newtons	0.225	poundforce	lbf
kPa	kilopascals	0.145	poundforce per square inch	lbf/in^2

* SI is the symbol for the International System of Units. Appropriate rounding should be made to comply with Section 4 of ASTM E380.

(Revised September 1993)

TABLE OF CONTENTS

LIST OF FIGURES

LIST OF FIGURES
(Continued)

LIST OF FIGURES
(Continued)

LIST OF TABLES

PROJECT SUMMARY

Background and Objectives

This final report documents the findings of a four and one-half year study of ***"Microdamage Healing in Asphalt and Asphalt Concrete."*** The study is identified as Task K in a larger overall study under the direction of Western Research Institute entitled ***"Fundamental Properties of Asphalts and Modified Asphalts."*** The study was sponsored by the Federal Highway Administration (FHWA) under contract number DTFH61-92-C-00170. Work in Task K was a joint effort between the Texas Transportation Institute (TTI) of Texas A&M University and the Department of Civil Engineering at North Carolina State University (NCSU).

The final report is divided, for reasons of readability and ease of documentation, into four volumes: (1) Microdamage Healing - Project Summary Report, (2) Evidence of Microdamage Healing, (3) Micromechanics Fatigue and Healing Model, and (4) Viscoelastic Continuum Damage Fatigue Model.

There were five primary study objectives:

1. Demonstrate that microdamage healing occurs and that it can be measured in the laboratory and in the field.
2. Confirm that the same fracture properties that control propagation of visible cracks control the propagation of microcracks, and determine the effects of microdamage healing on these fracture properties and basic fracture parameters.
3. Identify the asphalt constituents that influence microdamage and microdamage healing.
4. Establish appropriate correlations between microdamage and microdamage healing in the laboratory and in the field.
5. Predict the effect of microdamage healing on pavement performance and develop the appropriate constitutive damage models that account for the effects of microdamage healing on the performance of asphalt concrete pavement layers.

By satisfying the objectives of this research, the FHWA will be able to:

1. Establish the validity and significance of microdamage healing in flexible pavement design and analysis.
2. Identify how microdamage healing can be utilized in pavement design and analysis.
3. Maximize pavement performance life by selecting asphalt binders that match the level of microdamage healing to the level of traffic.

Volume 1: Microdamage Healing - Project Summary Report

Volume 1 is a summary report that chronicles the research highlights of the entire study.

Volume 1 describes the success of the project in addressing the project objectives as summarized in the following paragraphs.

The initial research objective was to demonstrate that healing occurs and can be measured both in the laboratory and in the field. Healing was verified on laboratory test samples, which demonstrated that dissipated pseudo-strain energy (DPSE) with each cycle of loading, which steadily decreased during cyclic, controlled-strain loading, was recovered after rest periods. The level and rate of the recovered DPSE varied in a logical manner corresponding to changes in the duration of the rest period and the temperature during the rest period. A parameter called the Healing Index (HI) was developed to quantify the magnitude of healing. Furthermore, a Micromechanics Fatigue and Healing Model (MFHM) was developed in this study based on the basic laws of fracture and microcrack growth. This model predicts the size distribution of microcracks and the growth of the microcracks as the fatigue process continues. The model, which is based on a relationship between stiffness loss during the fatigue process (due to microcrack damage) and the rate of change in DPSE, reveals a reduced average length of microcracks in the sample following rest periods. The MFHM model can be used to accurately calculate (by reverse calculation techniques) pertinent material properties and the rate of change in DPSE during the fatigue and healing process at temperatures below 25°C. However, the back-calculated pertinent material properties and the rate of change in DPSE cannot be accurately predicted using the MFHM at temperatures above about 25°C. This is because below 25°C, the change in damage during cyclic loading is almost all due to microcrack growth and healing. However, at the higher temperatures, plastic deformation occurs to a considerable extent, and plastic damage is not accounted for by the MFHM.

Convincing evidence of healing based on field data further verifies the occurrence of and ability to measure microdamage and healing. The stiffness of damaged roadways was found to recover or increase after rest periods where the stiffness was measured using in situ surface wave techniques. Experiments that verify healing were performed on U.S. 70 in North Carolina, the Minnesota Road Project (MnROAD) project, and the Accelerated Loading Facility in McLean, Virginia.

The second research objective, using the MFHM, which is based on fracture mechanics principles, confirm that the same fracture properties that control the propagation of visible cracks also control the propagation of microcracks and determine the effects of microdamage healing on the basic fracture properties and the fatigue life.

The third objective was to identify the asphalt constituents that influence microdamage and microdamage healing. Five asphalts ranging widely in aromatic, amphoteric, and wax contents were considered, and asphalts with low amphoteric and high aromatic contents were found to be better healers. However, the most important relationship between binder properties and healing was based on surface energy, which was shown to be fundamentally related to fracture and healing in a landmark study by Richard Schapery. More specifically, two components of surface energy (the polar and the non-polar component) were found to explain experimental data on the rate of early healing and the development of long-term healing.

The fourth objective was to establish appropriate correlations between microdamage and microdamage healing in the laboratory and in the field. This was accomplished as evidence verifies that a very significant level of recovery or healing occurs in the field following rest periods, and this level of recovery is in agreement with the magnitude of healing measured in the laboratory.

Finally, the project sought to predict the effect of microdamage healing on pavement performance and to develop an appropriate damage model. Two complementary approaches to the accomplishment of this objective were developed in this research. One was the development of the viscoelastic continuum damage mechanics model (CDM) and the second was the micromechanics fatigue and healing model (MFHM). The CDM can be used to assess fatigue life from either controlled-strain or controlled-stress fatigue experiments and the direct effects of rest periods (healing) on damage. Whereas the CDM offers an assessment of generic damage, the MFHM offers considerable insight into how material properties of the mixture affect fracture rate, healing rate, and the net rate of crack growth or fatigue, which is a balance between fracture rate and healing rate.

Volume 2: Evidence of Microdamage Healing

Volume 2 documents laboratory and field testing that provides the evidence that microdamage healing is real and measurable and that it has a significant impact on pavement performance.

Part of the laboratory experiments to evaluate the impact of rest periods were performed at North Carolina State University (NCSU). In these experiments, fatigue damage was induced through flexural beam experiments. Damage was recorded as the flexural stiffness of the beam became smaller during the flexural fatigue experiment and as the dynamic modulus of elasticity (as measured from impact resonance) became smaller. The experiment included two very different asphalt binders: AAD and AAM. The experiment clearly demonstrated that the rest periods introduced after fatigue damage allowed significant recovery in the flexural and dynamic modulus. The recovery was attributed to the healing of microcracks within the sample. The time of the rest period and the temperature of the sample during the rest period were found to significantly affect the degree of healing. The healing potentials of AAD and AAM asphalt cements were evaluated using four different indicators. Each indicator showed AAM to be a significantly better healer than AAD.

A separate series of laboratory testing was performed at Texas A&M University's Texas Transportation Institute (TTI). These tests consisted of controlled-strain haversine loading direct tensile tests and controlled-strain trapezoidal loading direct tensile tests. The change and rate of change in DPSE were recorded throughout the test and after rest periods introduced during the fatigue tests. The recovered DPSE after the rest period normalized by the DPSE before the rest period defined a Healing Index (HI) term used to quantify healing. Although healing was found to be dependent on the temperature of the mixture during the rest period and the length of the rest

period, it was also found to be highly dependent on the type of asphalt cement. Asphalt AAM was found to provide much better healing properties than asphalt AAD, which is in agreement with the work of NCSU where significantly different testing protocols were used.

A discussion is presented in Volume 2 that explains the importance of transforming the dissipated energy into pseudo-dissipated energy in order to accurately evaluate the relative ability of the various mixtures to heal. The transformation to pseudo-strain energy can be tedious and painfully slow. However, a linear transformation protocol is presented that is acceptably accurate and efficient. This protocol was used in this research to calculate pseudo-dissipated energies for the mixtures compared.

The TTI laboratory work demonstrated that several factors may influence the measure of microdamage healing apart from crack healing: molecular structuring or steric hardening, temperature confoundment, and stress relaxation during loading and rest periods. Each factor is discussed with respect to its role in influencing microdamage and microdamage healing. The conclusions are that: 1) molecular structuring is not of significance or importance for the rest periods and test protocols used in this study; 2) temperature increase upon loading or dissipation during rest periods was minimal in these experiments and had an insignificant impact on measured properties due to the nature of the test protocol, number of loading cycles used, and length of rest periods; and 3) stress relaxation is accounted for in the determination of the pseudo-strain energy data as they relate to microdamage healing.

The influence of several factors as they affect microdamage healing (the healing index) are discussed. These include the effects of low density polyethylene (LDPE) as an asphalt additive, the effects of age-hardening (including the effects of hydrated lime as an inhibitor of hardening), the effect of five different binders (exhibiting very different compositional properties), and the effect of different mixture types (dense graded mixtures versus stone mastic type mixtures).

The most notable finding presented in this volume is the difference in healing indices among the five virgin binders evaluated. A strong relationship between surface energy of the binder and the magnitude of healing and the rate of realization of maximum healing is presented. This relationship agrees with the fundamental (fracture mechanics-based) explanation of fatigue presented in Volume 3. In this fundamental relationship, the fatigue process is presented as a balance between the fracture during loading and healing or recovery during periods of rest.

Volume 2 completes the evidence of microdamage healing with convincing field evidence. Wave speed and attenuation measurements were made on in situ pavements. The stress wave test and analysis successfully detected fatigue damage growth and microdamage healing of asphalt pavements (at the FHWA's Turner-Fairbank Highway Research Center - Accelerated Loading Facility) with different asphalt layer thicknesses and viscosities and demonstrated the importance of microdamage healing during rest periods on pavement performance. The ability of stress wave testing to measure microdamage and healing in the field was further evaluated at the Minnesota Road Project (Mn/ROAD) on seven pavement test sections at the site. The results further

confirmed that the stress wave analysis can be used to monitor microdamage growth and healing in the field. The conclusion of the field study was that, although healing of asphalt concrete pavements in the field is more difficult to measure than in the controlled setting of a laboratory, it can be accurately detected using stress wave analysis. The fact that healing does occur in pavements in the field during rest periods suggests that the performance and service life of the pavement will be increased if rest periods are introduced, or if binders are used which heal more quickly and completely, or if binders are used that heal more quickly and completely.

Volume 3: Micromechanics Fatigue and Healing Model

Volumes 3 and 4 present two different ways of describing the fatigue cracking in mixes. In both volumes, the sample being tested is damaged. The two approaches differ in their ways of characterizing cracking. InVolume 3, it is assumed that all of the damage is due to cracking and obeys the fracture and healing laws that have been established for viscoelastic materials. In this approach the material properties that are relevant to these fracture and healing laws may be measured independently of the sample that is tested in fatigue. The resulting model of fatigue cracking and healing is the Micromechanics Fracture and Healing Model (MFHM). In Volume 4, the sample is assumed to suffer a generic "damage" with which no material properties are associated. Instead, model coefficients are found by analysis of the sample damage and healing data. The resulting model is the continuum damage model (CDM). In Volume 3 is a description of the test that were run and interpreted using the MFHM at 4°C, 25°C, and 40°C. At the lower temperatures (4°C and 25°C), the MFHM model was used to calculate the cohesive fracture and healing surface energies, which were measured independently using a Wilhemy Plate apparatus. The calculated and measured values matched well within reasonable experimental error. However, at 40°C, the calculated surface energies did not match the measured values, indicating that a mechanism other than fracture and healing was operating at the higher temperature. The most likely damage mechanism to operate at the higher temperature is plastic flow. This suggests that a continuum damage model (CDM) at the higher temperatures will probably be of a different form with different sets of model coefficients than what was found to fit the fracture and healing damage mechanism at the lower temperatures as discussed in Volume 4. The most likely dividing line between the fracture and healing mechanism and the plastic flow mechanism is the stress free temperature of the asphalt concrete mixture.

Three events occur simultaneously in asphalt mixtures under strain-controlled fatigue loading. These are relaxation, fracture, and healing. Relaxation of stress is a direct result of asphalt molecular structure. Fracture can be regarded as the growth of microcracks or macrocracks during loading, and healing is the recovery of the asphalt structure during rest periods. Healing is at least partly due to the recovery of bonding strength at the closure of fracture faces. The relaxation and healing mechanisms extend the performance life of asphalt mixtures while fatigue damage degrades their quality.

The theories of fracture mechanics are well established for time-independent materials, such as metals. However, analysis methods to characterize the behavior of time-dependent viscoelastic

materials are rare. A number of approximate interrelationships between linear elastic and viscoelastic properties have been developed; however, they are only applicable to quasi-static problems. Finding a closed-form solution to quantify the response of viscoelastic materials under general loading conditions is one of the objectives of a portion of the study described in this volume. A second objective of this portion of the research was to show that the same fracture properties that control the propagation of visible cracks control the propagation of microcracks.

It is a third objective to show that the microfracture and healing properties that can be calculated from the measured results of tensile fatigue tests match the cohesive fracture and healing properties of the asphalt binder that can be measured independently. It is this third objective which demonstrates closure: The microfracture and healing theory proposed in this report actually does predict the measured results.

An extended background review of the literature, which supports much of the development of the models presented in this volume, is presented in the Ph.D. dissertation of Chen [1997]. This volume presents a finite element model, which is used to calculate the fracture properties of asphalt mixtures and to calculate damage behavior (average crack length and density of crack distribution) during fatigue testing. The fracture properties and damage assessment is based on dissipated pseudo-strain energy, which is recorded throughout the test. Based on the microfracture and healing model, a fundamental relation of viscoelastic fracture was derived and is presented in this volume. This fundamental law is used to describe the rate or speed of fracture and the rate or speed of microfracture healing based on fundamental properties of the mixture and its components. The law defines the fatigue process as being a balance between the rate of fracture and the rate of healing. The fundamental relationship identifies component and global mixture properties that affect fracture and healing. Tests to measure these material properties show potential for development into specification tests. Among these are the surface energy tests for binders and aggregates and mixture tensile and compressive compliance tests. The reasonableness of the approach is demonstrated by the fact that the fundamental relationship of viscoelastic fracture mechanics was used to calculate fracture and healing surface energies from actual fatigue test dissipated pseudo-dissipated energy data and fundamental mixture fracture properties were calculated from these data. The calculated mixture surface energies were within a reasonable range of those measured separately for the binder and mixture as discussed in Volume 3.

The analytical methods presented in this volume demonstrate a reduction in average microcrack length following rest periods and that the same fundamental fracture parameters that influence macrocrack growth (fractures larger than about 7.5 mm) also control microcrack growth.

Volume 4: Viscoelastic Continuum Damage Fatigue Model of Asphalt Concrete With Microdamage Healing

A mechanistic approach to fatigue characterization of asphalt-aggregate mixtures is presented in this volume. This approach is founded on a uniaxial viscoelastic constitutive model that accounts for damage evolution under cyclic loading conditions. The elastic-viscoelastic correspondence principle is applied in order to evaluate damage growth and healing in cyclic loading separately from time-dependent characteristics of the material. The damage growth during loading cycles and healing during rest periods are modeled using work potential theory, a continuum damage theory based on thermodynamics of irreversible processes. Internal state variable formulation was used in developing the analytical representation model. Tensile uniaxial fatigue tests were performed in the controlled-strain mode with different strain amplitudes to determine model parameters. The resulting constitutive model successfully predicts the damage growth of asphalt concrete under monotonic loading at varying strain rates and damage growth and recovery due to complex loading histories, in both controlled-strain and controlled-stress modes, composed of randomly applied multi-level loading with different loading rates and varying durations of rest.

Fatigue lives of two different mixtures were predicted with reasonable accuracy using the constitutive model for the constant stress-strain amplitude cyclic loading histories with and without rest periods. A standard uniaxial fatigue test protocol is proposed by simplifying the experimental approach used in developing the constitutive model.

VOLUME SUMMARY

This volume documents the development of the micromechanics fracture and healing model (MFHM). This model is based on the assumption that all of the damage in the test sample is due to cracking and obeys the fracture and healing laws that have been established for viscoelastic materials. Therefore, the material properties that are relevant to these fracture and healing laws can be measured independently of the sample that is tested in fatigue.

The model is based on a relationship between the reduction in stiffness of a cylindrical sample of asphalt concrete subjected to cyclic direct tensile fatigue loading and the rate of dissipated pseudo-strain energy occurring during the cyclic loading. The relationship between stiffness reduction in the direction of axial loading (a measure of damage) and the rate of dissipated pseudo-strain energy is also affected by the basic Paris fracture properties and the global surface energy of the mixture.

The MFHM is shown to apply to mixtures tested at and below a test temperature of 25° C. This is because the relative damage in these samples is due to microcrack fracture and healing. On the other hand, samples tested at higher temperatures are subjected to considerable plastic damage, and crack growth theory could not adequately explain the accumulation of damage.

The MFHM is shown to accurately predict the rate of change in pseudo-strain dissipated energy as crack damage occurs in samples tested at temperatures below 25°C. The model also logically accounts for the effects of healing as it demonstrates a reduction in average microcrack size following rest periods.

VOLUME 3: MECHANISTIC APPROACH TO THE EVALUATION OF MICRODAMAGE AND MICRODAMAGE HEALING IN ASPHALT CONCRETE MIXTURES

CHAPTER 1: INTRODUCTION

Volumes 3 and 4 present two different ways of describing the fatigue cracking in mixes. In both volumes, the sample being tested is damaged. The two approaches differ in their ways of characterizing cracking. In this volume, it is assumed that all of the damage is due to cracking and obeys the fracture and healing laws that have been established for viscoelastic materials. In this approach the materials properties that are relevant to these fracture and healing laws may be measured independently of the sample that is tested in fatigue. The resulting model of fatigue cracking and healing is the micromechanics fracture and healing model (MFHM). In Volume 4, the sample is assumed to suffer a generic "damage" with which no material properties are associated. Instead, model coefficients are found by analysis of the samples' damage and healing data. The resulting model is the continuum damage model (CDM). Tests were run and interpreted using the MFHM at 4° C, 25°C and 40°C. At the lower temperatures (4°C and 25°C), the MFHM model was used to calculate the cohesive fracture and healing surface energies which were measured independently using a Wilhemy Plate apparatus. The calculated and measured values matched well within reasonable experimental error. However, at 40°C, the calculated surface energies did not match the measured values, indicating that a mechanism other than fracture and healing was operating at the higher temperature. The most likely damage mechanism to operate at the higher temperature is plastic flow. This suggests that a continuum damaged model (CDM) at the higher temperatures will probably be of a different form with different sets of model coefficients than what was found to fit the fracture and healing damage mechanism at the lower temperatures and is discussed in Volume 4. The most likely dividing line between the fracture and healing mechanism and the plastic flow mechanism is the stress free temperature of the asphalt concrete mixture.

Three events occur simultaneously in asphalt mixtures under strain controlled fatigue loading. These are relaxation, fracture, and healing. Relaxation of stress is a direct result of asphalt molecular structure. Fracture can be regarded as the growth of microcracks or macrocracks during loading, and healing is the recovery of the asphalt structure during rest periods. Healing is at least partly due to the recovery of bonding strength at the closure of fracture faces. The relaxation and healing mechanisms extend the performance life of asphalt mixtures while fatigue damage degrades their quality.

The theories of fracture mechanics are well established for time-independent materials, such as metals. However, analysis methods to characterize the behavior of time-dependent viscoelastic materials are rare. A number of approximate interrelationships between linear elastic and viscoelastic properties have been developed; however, they are only applicable to quasi-static problems. Finding a closed-form solution to quantify the response of viscoelastic materials under

general loading conditions is one of the objectives of a portion of the study described in this volume. A second objective of this portion of the research was to show that the same fracture properties that control the propagation of visible cracks control the propagation of microcracks.

It was a third objective to show that the microfracture and healing properties that can be calculated from the measured results of tensile fatigue tests match the cohesive fracture and healing properties of the asphalt binder that can be measured independently. It is this third objective that demonstrates closure: The microfracture and healing theory proposed in this report actually does predict the measured results.

An extended background review of the literature, which supports much of the development of the models presented in this volume, is presented in the Ph.D. dissertation of Chen (1997). This chapter presents a finite element model, which is used to calculate the fracture properties of asphalt mixtures and to calculate damage behavior (average crack length and density of crack distribution) during fatigue testing. The fracture properties and damage assessment is based on dissipated pseudo-strain energy, which is recorded throughout the test. Based on the microfracture and healing model, a fundamental relation of viscoelastic fracture was derived and is presented in this chapter. This fundamental law is used to describe the rate or speed of fracture and the rate or speed of microfracture healing based on fundamental properties of the mixture and its components. The law defines the fatigue process as being a balance between the rate of fracture and the rate of healing. The fundamental relationship identifies component and global mixture properties that affect fracture and healing. Tests to measure these material properties show potential for development into specification tests. Among these are the surface energy tests for binders and aggregates and mixture tensile and compressive compliance tests. The reasonableness of the approach is demonstrated by the fact that the fundamental relationship of viscoelastic fracture mechanics was used to calculate fracture and healing surface energies from actual fatigue test pseudo-dissipated energy data and fundamental mixture fracture properties calculated from these data. The calculated mixture surface energies were within a reasonable range of those measured separately for the binder and mixture as discussed in Volume 2.

The analytical methods presented in this volume demonstrate a reduction in average microcrack length following rest periods and that the same fundamental fracture parameters that influence macrocrack growth (fractures larger than about 7.5 mm) also control microcrack growth.

The remainder of this volume is divided into the following chapters:

Chapter 2 - A description of pseudo-strain analysis in a viscoelastic body,

Chapter 3 - A discussion of how uniaxial tensile fatigue testing was used and evaluated to achieve data for analysis of evaluation of the MFHM,

Chapter 4 - A description of the finite element model (FEM) for microcrack growth,

Chapter 5 - A discussion of the fundamental laws governing the rates of fracture and healing.

CHAPTER 2: PSEUDO-STRAIN ANALYSIS IN VISCOELASTIC BODY

In the quasi-static cases where separation of variables conditions prevail, the solution of boundary value problems may be obtained by special means. By separation of variables we mean the existence of the solution for surface and body force variables in the form:

$$u_i(x_i\ ,\ t) = u_i'(x_i)\ u(t) \tag{1}$$

$$\epsilon_{ij}(x_i\ ,\ t) = \epsilon_{ij}'(x_i)\ u(t) \tag{2}$$

$$\sigma_{ij}(x_i\ ,\ t) = \sigma_{ij}'(x_i)\ F(t) \tag{3}$$

In this case the Laplace transform simply changes the time domain to the s domain leaving the space dependence unchanged. Since this is linear, if the loading falls into groups of proportional loading and prescribed displacements, each with a different time dependence, they can be considered separately and superposed. The functions u(t) and F(t) are determined by:

$$\left(\frac{\partial^m}{\partial t^m} + a_{m-1}\frac{\partial^{m-1}}{\partial t^{m-1}} + \cdots + a_0\right) u(t) = \left(\frac{\partial^n}{\partial t^n} + b_{n-1}\frac{\partial^{n-1}}{\partial t^{n-1}} + \cdots + b_0\right) F(t) \tag{4}$$

The a's and b's define the characteristics of the material. With the initial condition that u(t) and its first (n-1) derivatives vanish at t = 0, the function u(t) depends only on F(t) and the properties of the material. The other characteristics of the problem do not enter into its determination.

In this research, two particular solutions based on Alfrey's theorem (1944) are detailed below. One is for asphalt cylinder specimens under trapezoidal strain-controlled loading and the other is for specimens under half-cubic-sine strain-controlled loading. There is a relaxation influence between the analytic functions u(t) and F(t). To get the basic functions for each sample, the testing program began with a simple tension and compression relaxation loading. Stresses and strains used in the evaluation of relaxation modulus were nominal stresses and strains; they are:

$$\sigma = P/A \tag{5}$$

and

$$\epsilon = u/L \tag{6}$$

where

P = load response,

A = cross -ection area of the cylinder sample regardless of the distribution of microcrack faces,

u = the displacement measured from the average reading of three vertical LVDTs attached to the sample, and

L = original height of the sample.

Pseudo Strain for Trapezoid Strain-Controlled Loading

Under the separation of variables conditions, the stress/pseudo-strain relation in the form of a hereditary integral can be calculated without space dependence. Pseudo strain for a constant strain rate monotonic loading case is determined from:

$$\epsilon^e = \frac{C}{E_R}\int_0^t E(\tau)\, d\tau \tag{7}$$

where $C = d\epsilon/dt$.

Following a superposition method developed by Lytton (1994), the trapezoidal strain loading falls into four groups of prescribed strains as shown in Figure 1. The pattern begins to repeat itself with each load cycle. During the first loading path of trapezoidal strain wave, the sample cannot distinguish whether the test is monotonic loading or cyclic loading. Therefore, the pseudo strain can be calculated from Equation (7). During the flat strain period of tensile stress relaxation, the superposition of the counter strain pattern gives:

$$\epsilon^e(t) = \frac{C}{E_R}\int_0^{t_1} E^+(\tau)\, d\tau = \epsilon^e_{max} \tag{8}$$

where

t_1 = the time of the increasing strain ramp,

$E^+(t)$ = the tensile relaxation modulus, and

E_R^+ = the reference modulus, which is an arbitrary constant.

For the first unloading ramp, the same practice yields:

$$\epsilon^e(t) = \frac{C}{E_R} \int_0^{t_1} E^+(\tau)\, d\tau - \frac{C}{E_R} \int_0^{t - t_2} E^-(\tau)\, d\tau \qquad (9)$$

where

t_2 = the time when unloading begins, and
$E^-(t)$ = the compressive relaxation modulus.

The pseudo strain for the compression relaxation period is:

$$\epsilon^e(t) = \frac{C}{E_R} \int_0^{t_1} E^+(\tau)\, d\tau - \frac{C}{E_R^-} \int_0^{t_3 - t_2} E^-(\tau)\, d\tau = \epsilon^e_{min} \qquad (10)$$

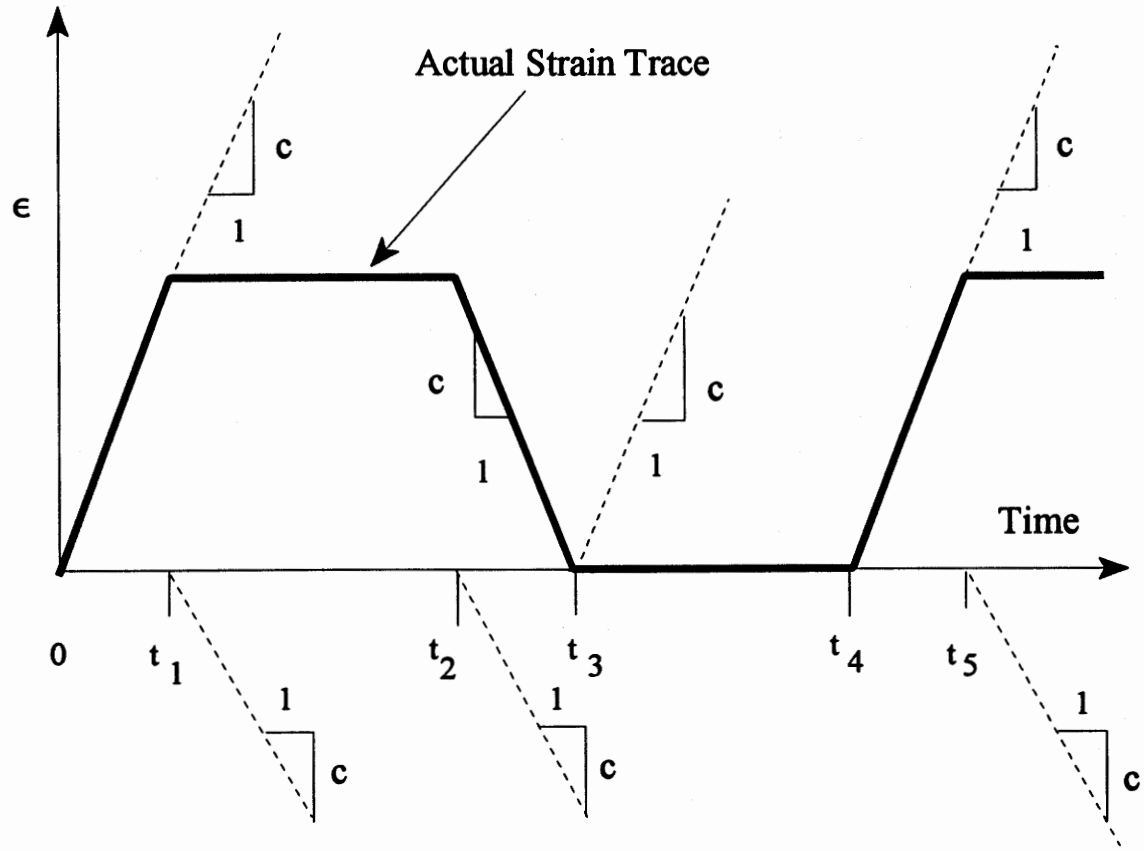

Figure 1. Superposed Strain Pattern for Trapezoid Strain Wave.

Pseudo Strain for General Loading Condition

When a viscoelastic medium is subjected to cyclic loading as shown in Figure 2, the strain history can be expressed as a series of a periodic functions $g_1(t)$. With zero initial conditions $g_1(0)=0$, the Laplace transform of function $g_1(t)$ is:

$$\mathcal{L}[g_1(t)] = \frac{\int_0^T e^{-st}\, g_1(t)\, dt}{1 - e^{-Ts}} \tag{11}$$

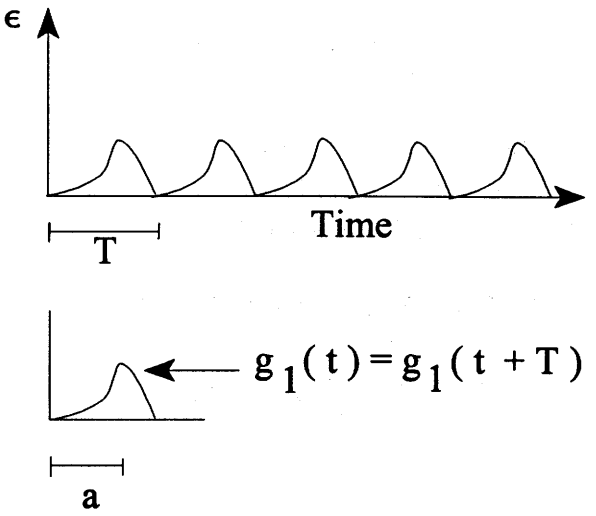

Figure 2. A Periodic Function $g_1(t)$ for Strain-Controlled Fatigue Loading.

and the Laplace transform of $g_1'(t)$ is:

$$\mathcal{L}[\, g_1'(t)\,] = s \cdot \mathcal{L}[\, g_1(t)\,] \tag{12}$$

Following the work of Schapery, pseudo strain can be of the form:

$$\epsilon^e(t) = \frac{1}{E_R} \int_0^t E(t-\tau)\, \frac{d\epsilon(\tau)}{d\tau}\, d\tau \tag{13}$$

After taking the Laplace transform, Equation (12) becomes:

$$\mathcal{L}[\ \epsilon^e(t)\ ] = \frac{1}{E_R}\ \mathcal{L}[\ E(t)\ ]\ \mathcal{L}[\ \epsilon'(t)\ ] \tag{14}$$

From Figure 2, the viscoelastic body during time period [0, a] is subjected to tensile loading. Equation (14) becomes:

$$\mathcal{L}[\ \epsilon^e(t)\ ] = \frac{1}{E_R}\ \mathcal{L}[\ E^+(t)\ ]\ \mathcal{L}[\ g'_1(t)\ ] \tag{15}$$

To transform Equation (15) back from the s domain to the time domain, the complex Laplace inversion technique (1976) is utilized:

$$\epsilon(t) = \sum \textit{residues of } \{\ \mathcal{L}[\epsilon^e\ (t)]\ e^{st}\ \} \textit{ at each of its poles} \tag{16}$$

During time period [a, T], the viscoelastic body is under compressive loading and the responding relaxation modulus will be different than the one in tension. As shown in Figure 2, the superposition method can be applied to describe the material behavior.

The pseudo-strain equation after subtracting and adding the counter-strain patterns is:

$$\epsilon^e(t)=\frac{1}{E_R}\{\int_0^t E^+(\tau)g_1'(t-\tau)d\tau-\int_0^{t^*}E^+(\tau)g_2'(t^*-\tau)d\tau+\int_0^{t^*}E^-(\tau)g_2'(t^*-\tau)\ d\tau\} \tag{17}$$

where $g_2(t^*)$ is a new periodic function and $t^* = t - a$ as defined in Figure 3(b).

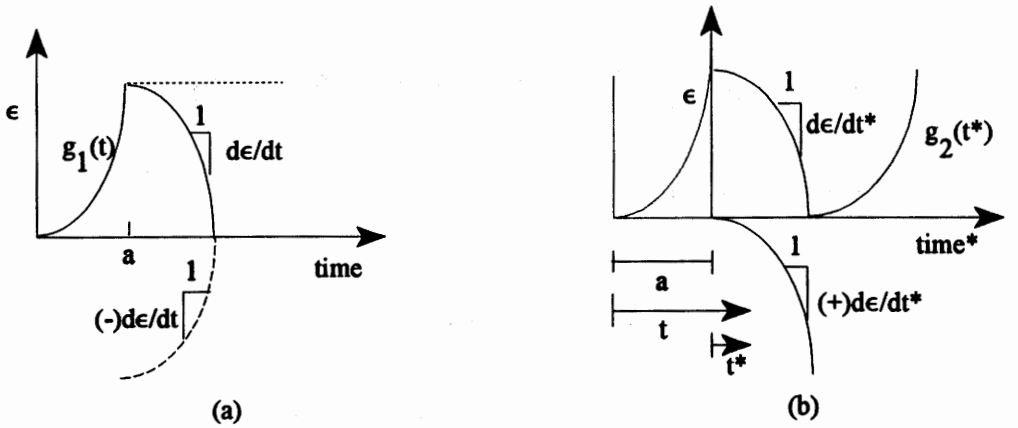

Figure 3. Superposition Method for General Loading Condition: (a) Subtraction with Tensile Relaxation Modulus E^+, (b) Addition with Compressive Relaxation Modulus E^-.

The initial condition of $g_2(t^*)$ may not be zero and the Laplace transform of Equation (17) is:

$$\mathcal{L}[\epsilon^e(t)]=\frac{1}{E_R}\{\ \mathcal{L}[E^+ * g_1'(t)]-\mathcal{L}[E^+ * g_2'(t^*)]+\mathcal{L}[E^- * g_2'(t^*)]\ \} \tag{18}$$

where

$\epsilon^e(t)$ is the sum of residues of $\mathcal{L}[\epsilon^e(t)]e^{st}$ at each of its poles.

The pseudo strain during time period [T, T+a] is:

$$\begin{aligned}\epsilon^e(t)=\frac{1}{E_R}\{&\int_0^t E^+(\tau)g_1'(t-\tau)d\tau-\int_0^{t^*}E^+(\tau)g_2'(t^*-\tau)d\tau+\int_0^{t^*}E^-(\tau)g_2'(t^*-\tau)d\tau\\&-\int_0^{t^{**}}E^-(\tau)g_1'(t^{**}-\tau)d\tau+\int_0^{t^{**}}E^+(\tau)g_1'(t^{**}-\tau)d\tau\ \}\end{aligned} \tag{19}$$

where $t^{**} = t^{(2)} = t - T$.

The Laplace transform of Equation (19) becomes:

$$\mathcal{L}[\epsilon^e(t)]=\frac{1}{E_R}\{\mathcal{L}[E^+ * g_1']-\mathcal{L}[E^+ * g_2']+\mathcal{L}[E^- * g_2']-\mathcal{L}[E^- * g_1']+\mathcal{L}[E^+ * g_1']\} \tag{20}$$

The Laplace transform of pseudo strain for time period [T+a, 2T] is analogous to that for time period [a, T]:

$$\begin{aligned}\mathcal{L}[\epsilon^e(t)]=\frac{1}{E_R}\{&\mathcal{L}[E^+ * g_1']-\mathcal{L}[E^+ * g_2']+\mathcal{L}[E^- * g_2']-\mathcal{L}[E^- * g_1']+\mathcal{L}[E^+ * g_1/]\\&-\mathcal{L}[E^+ * g_2']+\mathcal{L}[E^- * g_2']\}\end{aligned} \tag{21}$$

Therefore, the Laplace transform can be expressed according to the time period as:

(a) for time period [iT, a + iT], i = 0, 1, 2 ...

$$\mathcal{L}[\epsilon^e(t)]=\frac{(i+1)\{\mathcal{L}[E^+ * g_1']-\mathcal{L}[E^- * g_1']\}+(i)\{\mathcal{L}[E^- * g_2']-\mathcal{L}[E^+ * g_2']\}+\mathcal{L}[E^- * g_1']}{E_R} \tag{22}$$

(b) for time period [a +iT, (i+1)T], i = 0, 1, 2 ...

$$\mathcal{L}[\epsilon^e(t)]=\frac{(i+1)\{\mathcal{L}[E^+ * g_1']-\mathcal{L}[E^- * g_1']\}+(i+1)\{\mathcal{L}[E^- * g_2']-\mathcal{L}[E^+ * g_2']\}+\mathcal{L}[E^- * g_1']}{E_R} \tag{23}$$

Equations (22) and (23) are schematically illustrated in Figure 4.

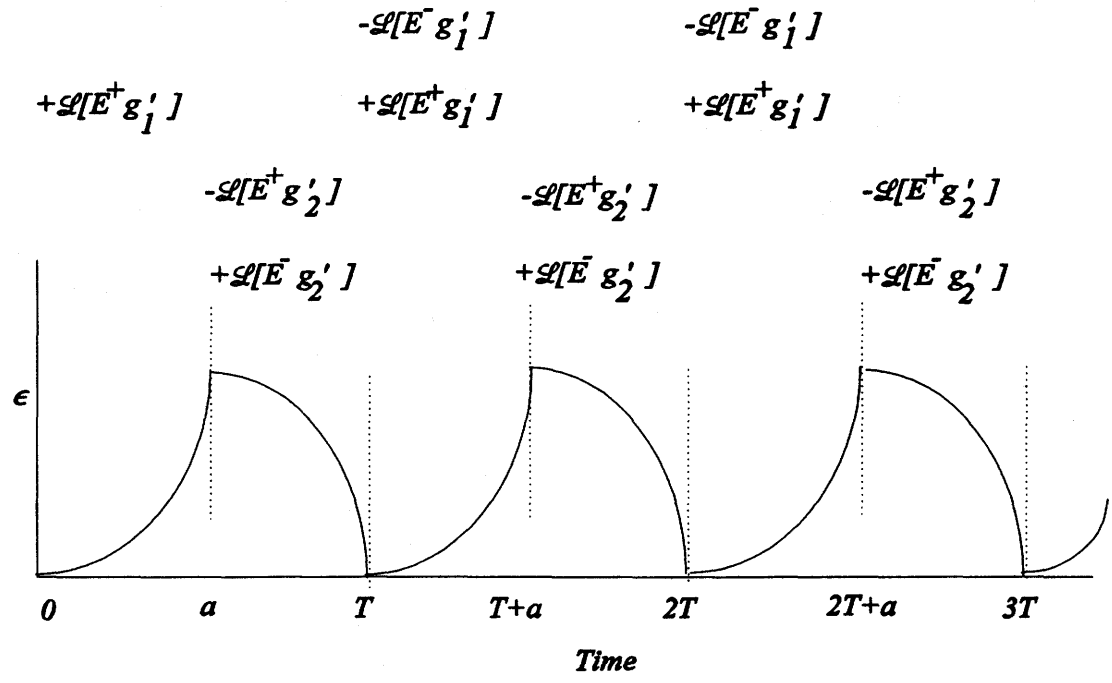

Figure 4. Laplace Transform of Pseudo Strain.

If the tension and compression relaxation modulus happen to be the same, Equations (22) and (23) can be reduced and the pseudo strain becomes:

$$\epsilon^e(t) = \sum residues\ of\ \{\frac{\mathcal{L}[E^+] \cdot \mathcal{L}[g'_1] \cdot e^{st}}{E_R}\}\ at\ each\ of\ its\ poles \qquad (24)$$

Equation (24) is derived for viscoelastic bodies that are initially undisturbed. With the same technique, problems with non-zero initial conditions are also well suited as long as Equation (22) is modified by adding a negative value of $g_1(0)$.

CHAPTER 3: UNIAXIAL FATIGUE TESTS

Two ways to express pseudo strains are derived in the previous chapter: the time integral of relaxation modulus and the residue sum of $\mathcal{L}[\epsilon^e(t)]e^{st}$. To utilize these two methods, two loading types of uniaxial fatigue tests were performed on asphalt mix cylinder specimens. They are trapezoidal strain-controlled loading and half-cubic-sine strain-controlled loading. The loading periods, alternated with rest periods, were applied during each fatigue test to simulate actual conditions of a pavement system. The loading and rest periods are schematically illustrated in Figure 5.

Study of Trapezoid Strain Loading Tests

The specimen configuration and trapezoidal strain loading wave are plotted in Figure 6. Three vertical LVDTs were placed to measure the loading response within the middle one third height of sample. The fatigue test consisted of several loading periods and rest periods. Each loading period consisted of 23 loading cycles. A rest period was incurred between two loading periods. These rest periods were 32 minutes between loading periods 1 and 2, 16 minutes between periods 2 and 3, 8 minutes between periods 3 and 4, 4 minutes between periods 4 and 5, 2 minutes between periods 5 and 6, 1 minute between periods 6 and 7, and 30 seconds between periods 7 and 8. The testing design required the establishment and definition of three characteristics: the loading wave form, the selection of rest period lengths, and the target maximum and minimum strain values. Details of the testing protocol and data acquisition are discussed in Volume 2.

The strain wave function was designed to approximate a step function, but with a sufficient ramp for accurate documentation and characterization of the material reaction during loading and unloading paths. This was accomplished using a hydraulic feedback system controlled by an average circuit connected to the three LVDTs. The wave form consisted of a 0.5-second ramp to the maximum strain, which was held for 10 seconds. Then a 0.5-second ramp was applied down to a slight compressive strain, which was also held for 10 seconds before the cycle was repeated.

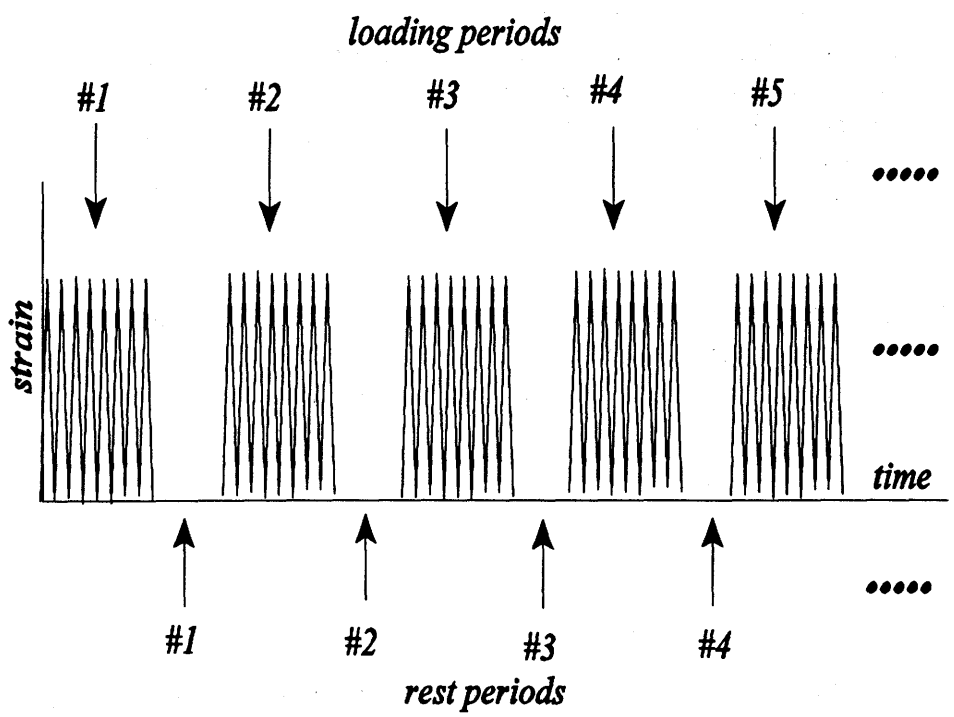

Figure 5. Schematic Illustration of Loading and Rest Periods.

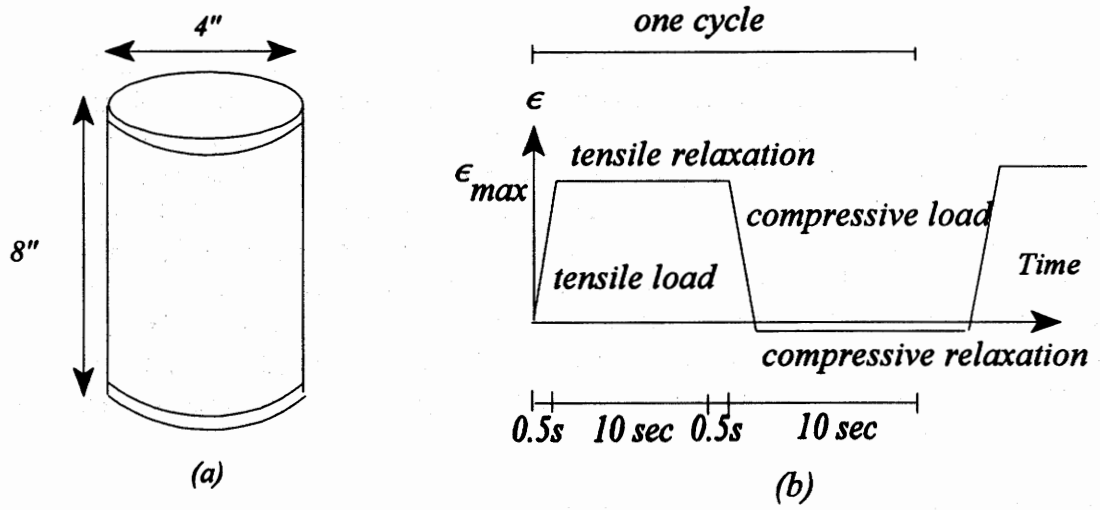

Figure 6. Trapezoid Strain-Controlled Loading Tests: (a) Specimen Configuration, (b) Strain Loading Wave.

Theoretically, each fatigue test could be performed at the same maximum strain level in hopes of achieving results that could be used to compare the effects of different binders, rest periods and temperatures. However, due to the variation in asphalt properties with temperature and data resolution settings of the machine system, different levels of the maximum strain were applied. The minimum strain was applied in each test to place the fracture surfaces in contact with each other but without significant load.

Relaxation Modulus

Prior to each fatigue test, a simple tensile and compressive relaxation loading was performed. These data serve as a valuable reference in calculating pseudo strains. Usually, the tensile and compressive relaxation moduli for each specimen can be represented in the form of a generalized power law:

$$E^{+}(t) = E_0^{+} + E_1^{+}\, t^{-m^{+}} \tag{25}$$

$$E^{-}(t) = E_0^{-} + E_1^{-}\, t^{-m^{-}} \tag{26}$$

where E_0^+, E_1^+, and m^+ are regression constants for the tensile relaxation modulus, and E_0^-, E_1^-, and m^- are regression constants for the compressive relaxation modulus. However, a simple way to fit the data mix as shown in Figure 7 is to use a pure power law:

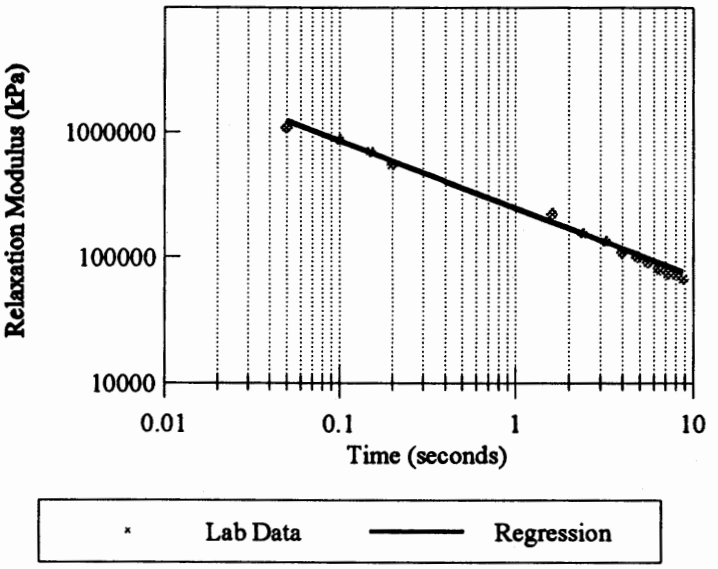

Figure 7. Tensile Relaxation Modulus for Sample M/DG/25 at 25°C. (The sample identification is explained in Volume 2. M is for asphalt AAM, DG is for a dense-graded mix, and 25 is the sample number.)

$$E^{+}(t) = E_1^{+}\, t^{-m^{+}} \tag{27}$$

$$E^{-}(t) = E_1^{-}\, t^{-m^{-}} \tag{28}$$

A linear regression analysis was performed between log[E(t)] and log(t), and the sum of squares of error was calculated. The regression results for each specimen are shown in Table 1. These material parameters may be applied to the fundamental relation of fracture mechanics and will be discussed further in the next section.

Table 1. Results of Relaxation Moduli for Tested Specimens.

Sample	E_1^+ (kPa)	m^+	E_1^- (kPa)	–	Temp.(°C)
M/DG/19	415796	0.460	290762	0.572	25
M/DG/25	252467	0.541	212876	0.590	25
M/DG/21	4702	0.629	6274	0.460	40
D/DG/17	4205	0.618	4440	0.536	40
F/DG/4	23449	0.716	28524	0.604	25
F/DG/6	79851	0.488	48685	0.555	25
B/DG/4	16789	0.537	18209	0.439	25
B/DG/3	49547	0.426	30503	0.507	25
B/DG/5	48761	0.461	30917	0.532	25
F/DG/2	65109	0.567	53491	0.606	25
F/FG/3	63323	0.530	42045	0.599	25
B/DG/2	703	0.620	558	0.520	40
M/DG/1	407439	0.433	344625	0.524	22.2
M/DG/3	382045	0.431	333855	0.498	22.2
D/DG/11	45562	0.553	75748	0.394	22.2
D/DG/12	51953	0.467	71618	0.365	22.2

Reference Modulus and Dissipated Pseudo-Strain Energy

The advantage of introducing a reference modulus E_R is that the pseudo-strains can be related to stresses through Hooke's law. If E_R is any arbitrary constant, the pseudo-strain energy stored in the specimen during the tensile loading path can have as many values as possible. It violates the first law of thermodynamics, which says there is a net decrease in energy when a system goes from a non-equilibrium to equilibrium state. To adjust for those inadequacies and still demonstrate Schapery's definition, the reference modulus E_R will be proposed in the following form:

$$\epsilon^e(t) = \frac{\sigma(t)}{E_R} \tag{29}$$

where E_R is a peculiar constant such that the maximum tensile pseudo-strain ϵ^e_{max} for each loading

cycle is equal to the maximum tensile strain ϵ_{max} designed in the fatigue test. The results of reference modulus, E_R , calculated for tested specimens are shown in Table 2.

Table 2. Results of Reference Modulus for Tested Specimens.

Sample	ϵ_{max} (millistrain)	σ_{max} (kPa)	E_R (kPa)
M/DG/19	0.3085	469	913587
M/DG/25	0.6150	689	563321
M/DG/21	2.8417	200	18106
D/DG/17	2.8453	186	19099
F/DG/4	1.9366	351	72631
F/DG/6	1.9633	598	160101
B/DG/4	1.9603	203	38308
B/DG/3	1.9649	358	92186
B/DG/5	1.9440	379	96150
F/DG/2	1.9550	599	152476
F/FG/3	1.9550	541	142864
B/DG/2	19.4540	204	1944
M/DG/1	0.3459	514	1565165
M/DG/3	0.3606	482	1385895
D/DG/11	0.3637	116	284556
D/DG/12	0.3385	94	238222

Data from sample M/DG/19 from the first three loading cycles are used to illustrate the material response under fatigue loading. Figure 8 presents the typical hysteresis loops.

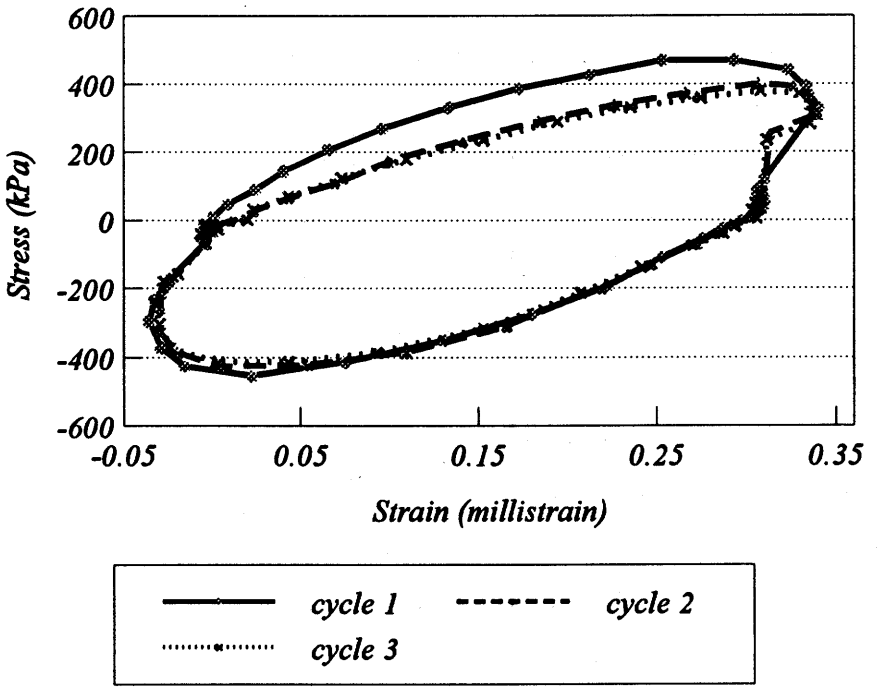

Figure 8. Stress-Strain Curves from M/DG/19 Tested at 25° C.

By applying Equations (8), (9), and (10) discussed previously, the corresponding stress/pseudo-strain curves are plotted in Figure 9. This technique was applied to analyze each fatigue test data set. With the proposed E_R, the tensile pseudo-strain energy has the same magnitude as the tensile strain energy and the determination of E_R for each specimen becomes clear. It will be shown in the next section that each E_r is extremely important in determining the fracture surface energy density, Γ.

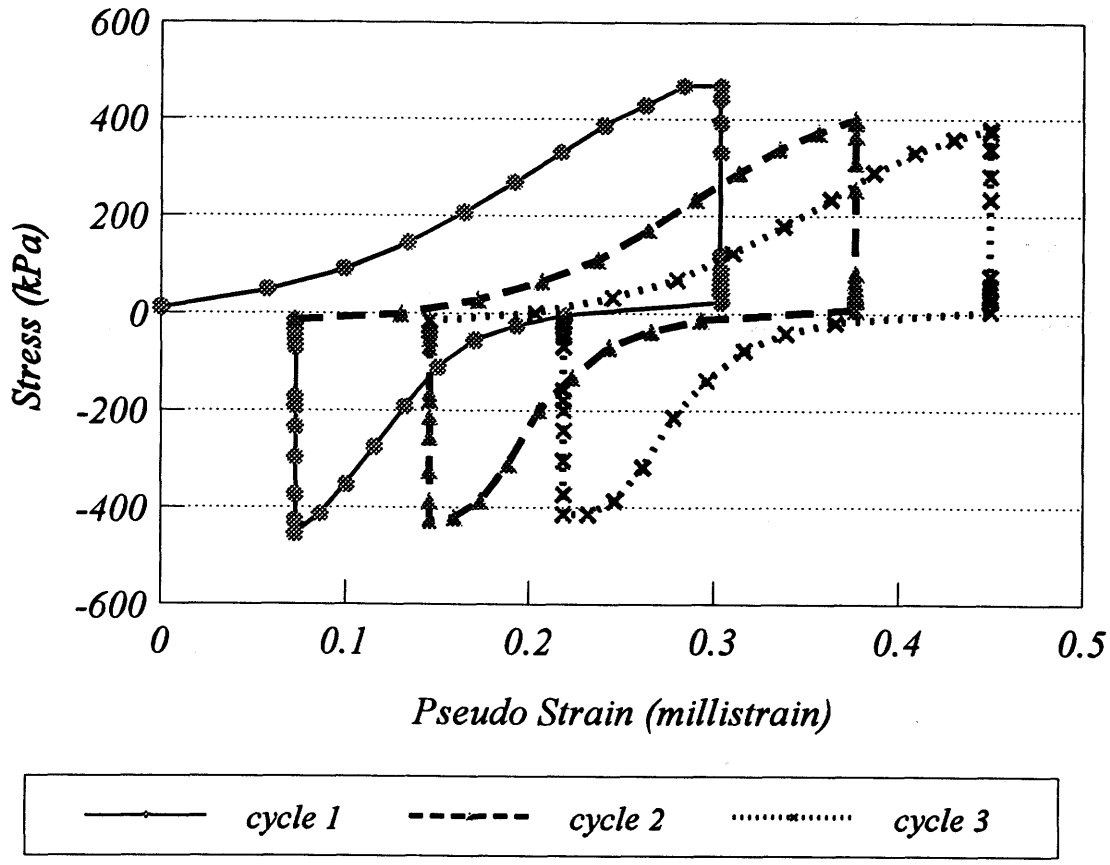

Figure 9. Stress/Pseudo-Strain Curves with Proposed E_R for M/DG/19.

After shifting the beginning points of each stress/pseudo-strain curve to the origin, the stress paths of mix M/DG/19 for the first four cycles are plotted in Figure 10. Note that this test is performed at a low target strain level in order to make sure that most of the material damage is through microcrack growth. When microcrack lengths increase with the loading cycle number, the effective thickness of each mix layer decreases and the stress increases. This is similar to the phenomenon of mastic film tests. The thinner the film thickness is, the stiffer the bitumen is (1968).

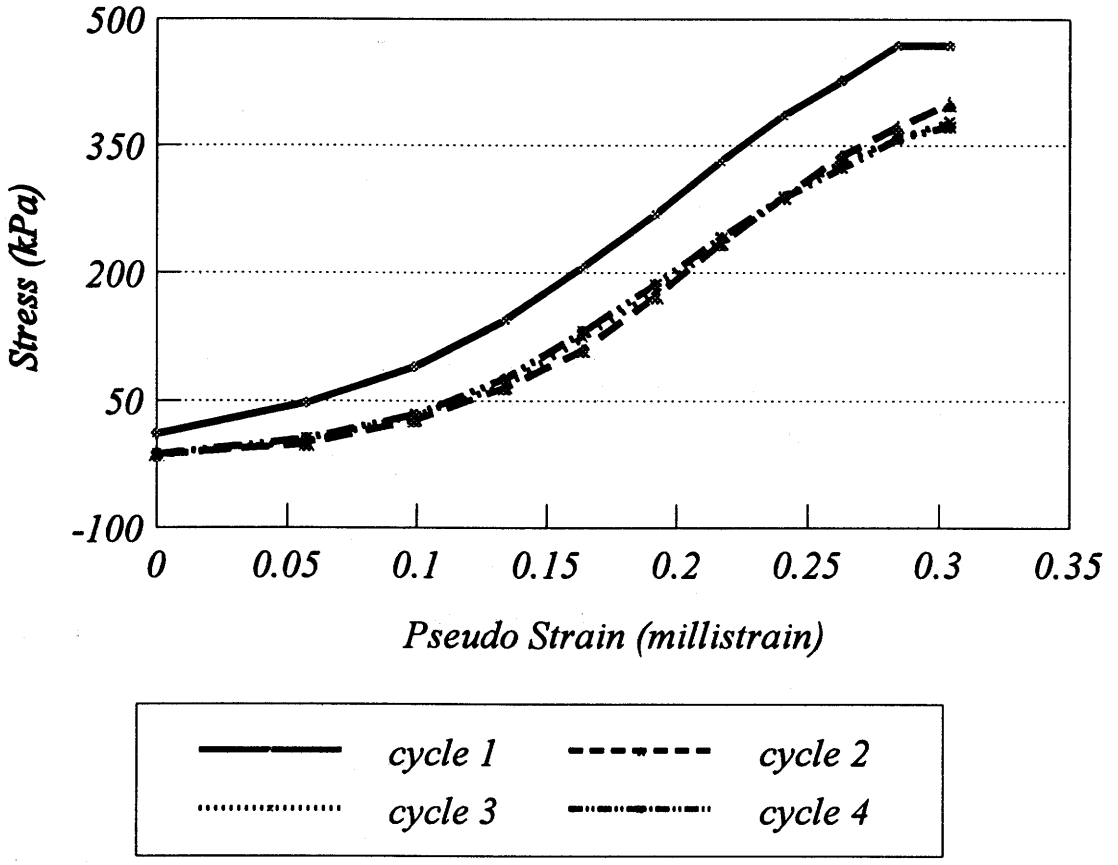

Figure 10. Stress Paths of M/DG/19 for the First Four Cycles.

Figures 11 through 14 are examples of pseudo-strain energy plotted for mix M/DG/19. The increase-drop-increase pattern of pseudo-strain energy is found in each analysis. This is believed to be an indication of the development of macrocracks from the coalescence of microcracks during the strain-controlled tests.

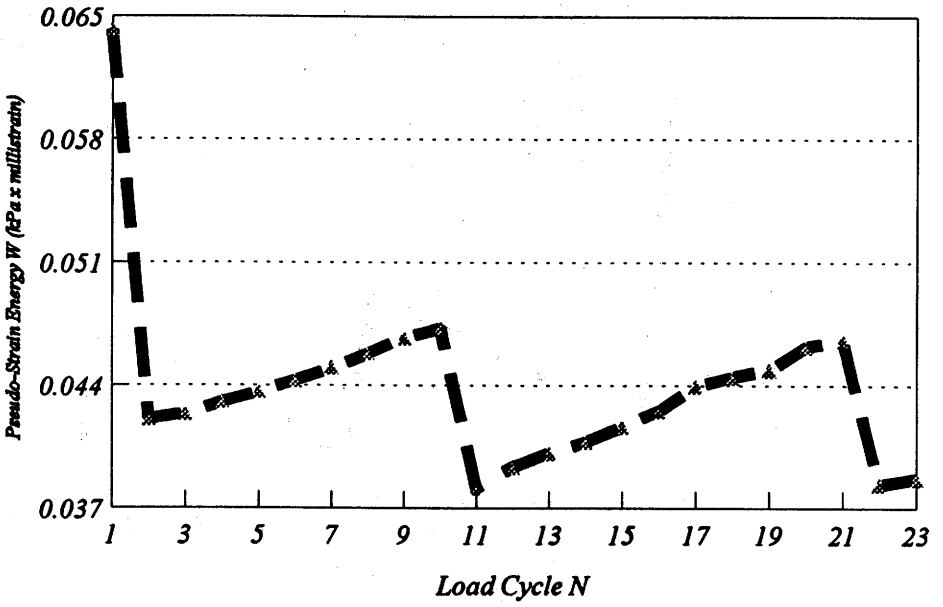

Figure 11. Pseudo-Strain Energy vs. Load Cycle of M/DG/19 During Load Period 1.

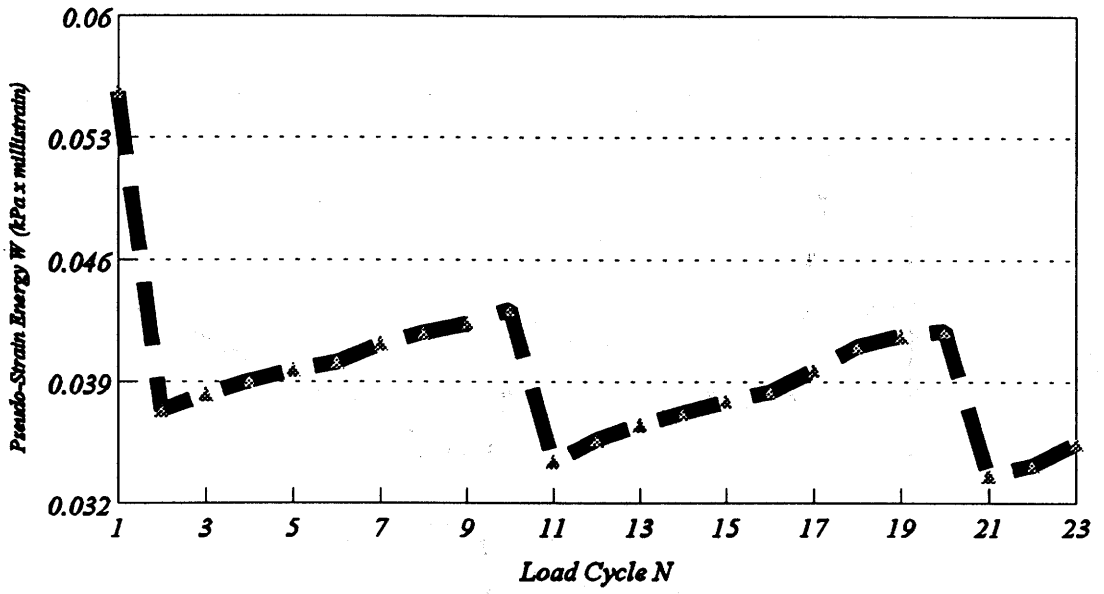

Figure 12. Pseudo-Strain Energy vs. Load Cycle of M/DG/19 During Load Period 2.

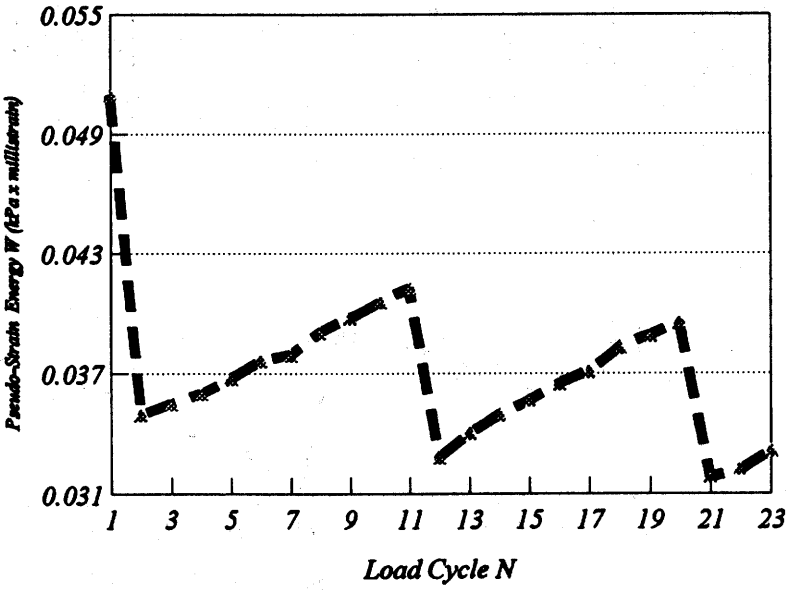

Figure 13. Pseudo-Strain Energy vs. Load Cycle of M/DG/19 During Load Period 3.

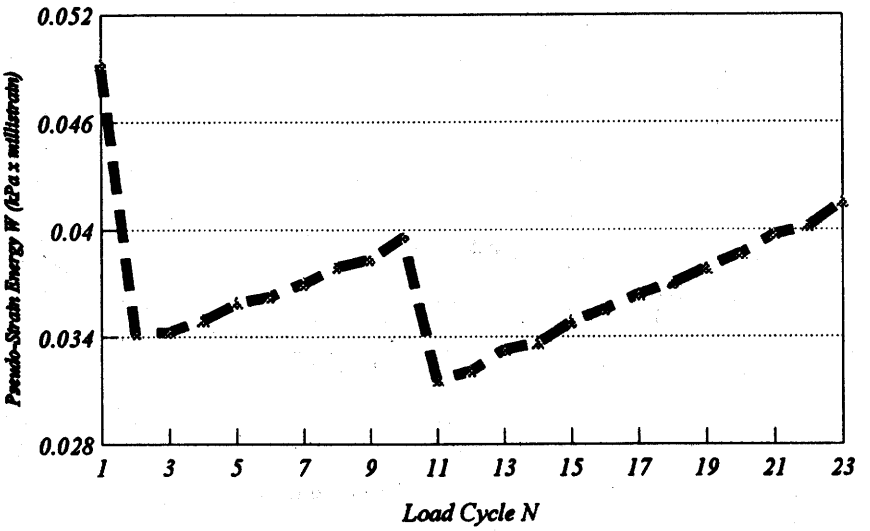

Figure 14. Pseudo-Strain Energy vs. Load Cycle of M/DG/19 During Load Period 4.

The patterns of change of pseudo-dissipated energy, W, with the number of load cycles shows a sawtooth pattern. For a number of consecutive load repetitions, the value of W rises smoothly and then suddenly, after one load application, the value of W drops sharply downward and then begins its slow rise again, normally on the same slope it was before the drop. This pattern is explained in the following way.

Microcracks grow as the rate of change of dissipated pseudo-strain energy, $\frac{dW}{dN}$, grows. So the steady rise of the W-vs-N curve between the sharp drops reflects the steady growth of microcracks. The pseudo-strain energy is expressed in units of mm-N/mm^3 or similar units, meaning that it is the pseudo-strain energy that is being dissipated per unit of volume of the sample being tested. The sharp drops in this quantity indicate that a crack area that is not a microcrack has suddenly opened up and some of the dissipated energy has been used to satisfy the surface energy requirements of the newly cracked area.

The size of the crack that opens to cause a precipitous drop in dissipated pseudo-strain energy is of macro-crack length with a diameter equal to or greater than roughly 7.5 mm. After this explosive appearance of a single macrocrack, the growth of microcracks, which are distributed throughout the volume of the sample, continues at steady pace. Thus, although there are interruptions in the W-vs-N curve caused by the sudden appearance of a single "macrocrack" or visible crack, the curve of $\frac{dW}{dN}$, the rate of change of dissipated pseudo-strain energy, is a smooth curve that follows the form

$$\frac{dW}{dN} = 2bN \; e^{a+bN^2} \tag{30}$$

This integrates into the W-vs-N curve

$$W = e^{a+bN^2} \tag{31}$$

This is a form of equation that leaves out the sharp drops of W upon the sudden formation of a macrocrack, but is entirely consistent with the steady growth of distributed microcracks as a function of the rate of change of dissipated pseudo-strain energy, $\frac{dW}{dN}$. When a sufficient number of these microcracks form, they too, begin to grow and the process of "crack propagation" begins. There is, in fact, no real distinction between the two processes of crack initiation and crack propagation except that the propagating cracks are larger (of visible size) and begin to use up the dissipated pseudo-strain energy at an increasing rate. An artificial distinction

can be made between the two processes to say that crack propagation begins when the steady growth

of $\frac{dW}{dN}$ ends and an accelerating rate begins. This measured value of $\frac{dW}{dN}$ is used in analyzing the laboratory tests that were made to determine the material properties that are related to microcracking. This use of the measured rate of change of dissipated pseudo-strain energy is explained subsequently on pages 38- 45 and particularly in equations (60) through (74).

Study of Half-Cubic-Sine Strain-Loading tests

A Closed-Form Solution for Pseudo Strain

The specimen configuration and half-cubic-sine strain loading wave are presented in Figure 15. The loading history is repeated with a 0.25-second half-cubic-sine wave and 0.35-second resting period. The results of four specimens (sample ID: M/DG/1, M/DG/3, D/DG/11 and D/DG/12) are discussed. The periodic function $g_1(t)$ can be defined as:

$$g_1(t) = \begin{matrix} \epsilon_{max} [\ \sin(4\pi t)\ ]^3 & 0.00\text{sec} \le t < 0.25\text{sec} \\ 0 & 0.25\text{sec} \le t < 0.60\text{sec} \end{matrix} \qquad (32)$$

During the time period [0 sec, 0.125 sec], the Laplace transform of tensile relaxation modulus $E^+(t)$ is:

$$\mathcal{L}[E^+(t)] = E_1^+ \Gamma(1 - m^+)\ s^{m^+ - 1} \qquad (33)$$

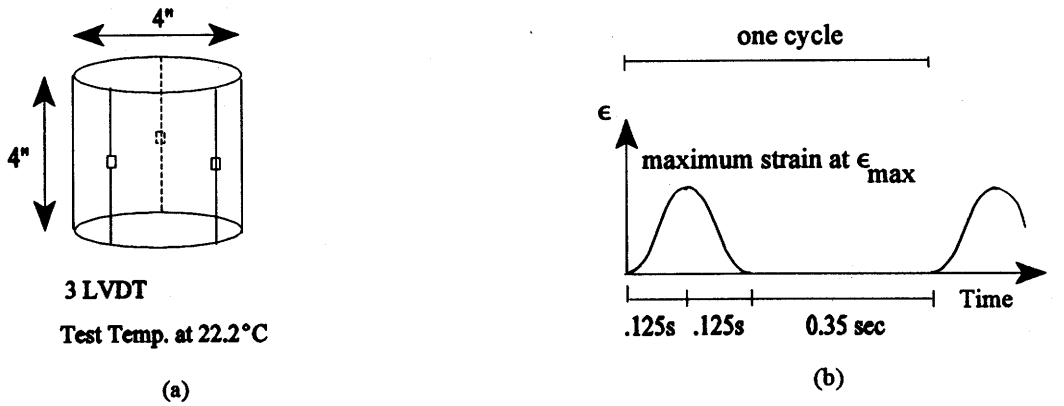

Figure 15. Half-Cubic-Sine Loading Tests: (a) Specimen Configuration, (b) Strain-Loading Wave.

and the Laplace transform of pseudo strain becomes:

$$\mathcal{L}[\epsilon^e(t)]=\frac{384\pi^3}{E_R}E_1^+\epsilon_{max}\Gamma(1-m^+)s^{m^+-1}\frac{(s+se^{-0.25s})}{(s^2+16\pi^2)(s^2+144\pi^2)(1-e^{-0.6s})} \tag{34}$$

Equation (34) has four first-order poles at ±4πi, ±12πi and infinitely many other first-order poles at (±10nπ/3i) where n=1, 2, . . ., ∞.

At the pole s = -4πi, the residual of Equation (34) is:

$$\lim_{s\to -4\pi i}\frac{384\pi^3}{E_R}E_1^+\epsilon_{max}\Gamma(1-m^+)\frac{(s+4\pi i)(s+se^{-0.25s})s^{m^+-1}e^{st}}{(s+4\pi i)(s-4\pi i)(s^2+144\pi^2)(1-e^{-0.6s})}=0 \tag{35}$$

At the pole s = 4πi, the residual is:

$$\lim_{s\to 4\pi i}\frac{384\pi^3}{E_R}E_1^+\epsilon_{max}\Gamma(1-m^+)\frac{(s-4\pi i)(s+se^{-0.25s})s^{m^+-1}e^{st}}{(s-4\pi i)(s+4\pi i)(s^2+144\pi^2)(1-e^{-0.6s})}=0 \tag{36}$$

Similarly, the residuals are zeros for the poles at s = 12πi and s = -12πi, respectively.

At the pole s = 10nπ/3i, the residual is [The indeterminacy is evaluated by L'Hospital's rule]:

$$\frac{31104\pi^3}{E_R}E_1^+\epsilon_{max}\Gamma(1-m^+)\frac{(1+e^{-\frac{2.5n\pi}{3i}})(\frac{10n\pi}{3i})^{m^+}e^{\frac{10n\pi}{3i}t}}{(86.4\pi^2-60n^2\pi^2)(1296\pi^2-100n^2\pi^2)} \tag{37}$$

and at the pole s = -10nπ/3i, the residual is:

$$\frac{31104\pi^3}{E_R}E_1^+\epsilon_{max}\Gamma(1-m^+)\frac{(1+e^{\frac{2.5n\pi}{3i}})(-\frac{10n\pi}{3i})^{m^+}e^{-\frac{10n\pi}{3i}t}}{(86.4\pi^2-60n^2\pi^2)(1296\pi^2-100n^2\pi^2)} \tag{38}$$

The pseudo strain is the sum of the total residuals:

$$\epsilon^e(t) = q\sum_{n=1}^{\infty}(\frac{10n\pi}{3})^{m^+}\frac{[\cos(\frac{10n\pi t}{3}+\frac{m^+x\pi}{2})+\cos(\frac{10n\pi t}{3}-\frac{2.5n\pi}{3}+\frac{m^+x\pi}{2})]}{(86.4\pi^2-60n^2\pi^2)(1296\pi^2-100n^2\pi^2)} \tag{39}$$

where $q = [62208\pi^3 E_1^+ \epsilon_{max} \Gamma(1-m^+)]/E_R$, and $\pm i = \cos\frac{x\pi}{2} \pm i\sin\frac{x\pi}{2}$, x = 1, 5, 9, ..., 41.

For comparison, the pseudo-strain solution from Schapery's approximate inversion is:

$$\epsilon^e(t) = \frac{384\pi^3 E_1^+ \epsilon_{max} \Gamma(1-m^+)}{E_R} \left| \frac{(s+se^{-0.25s})s^{m^+}}{(s^2+16\pi^2)(s^2+144\pi^2)(1-e^{-0.6s})} \right|_{s=\frac{1}{2t}} \quad (40)$$

Results and Discussion

The stress versus pseudo-strain curves obtained from three methods [the results of numerical integration, s = 1/2t, and Equation (39) with n up to 5] for each specimen are plotted in Figures 16 through 19. Although Schapery's approximate method is very easy, its accuracy will strongly depend on the assumption that the loading history is rather smooth. It is inadequate for half-cubic-sine strain-controlled loading. Figures 16 through 19 also show that the sum up to n = 5 will be accurate enough to represent the pseudo-strain history. The closed-form solution has the advantages of being able to be used in a spreadsheet calculation and of saving computer memory.

If the geometry and material properties of a cylindrical specimen are symmetric about its middle surface, according to Equation (39), the cylinder can be viewed as infinite layers combined in a series mode as shown in Figure 20. All layers are perfectly bonded together and interface slip is not allowed. The concept of infinite layers in a series mode is consistent with the study of trapezoidal strain loading tests in which the stress increases as the result of each asphalt layer getting thinner.

In this research, the closed-form solution for the hereditary integral is demonstrated through pseudo strains but the idea can be applied to pseudo stresses. Following the approach developed by Schapery, the hereditary integral can be symbolized by:

$$\{E\ df\} = E_R^{-1} \int_0^t E(t-\tau,t)\frac{\partial f}{\partial \tau} d\tau \quad (41)$$

or

$$\{D\ df\} = E_R \int_0^t D(t-\tau,t)\frac{\partial f}{\partial \tau} d\tau \quad (42)$$

After recognizing the periodic functions for strain-controlled loading conditions (such as constant-strain rate monotonic loading, constant-strain rate simple loading, pulse loading, and multi-level loading) or stress-controlled loading conditions (such as creep compliance loading, trapezoid stress wave loading, and sinusoidal stress-controlled loading), the closed-form solution can be

modified easily by replacing the old Laplace transform of the periodic function with a new one. Then the complex inversion method is used to determine the time-independent response. The derivation of a closed-form solution might be cumbersome, but it can be avoided by using tests in which the loading patterns and time steps are designed to reduce the level of complication. An example of the results of dissipated pseudo-strain energy for the haversine strain controlled tests are plotted in Figures 21, 22, and 23.

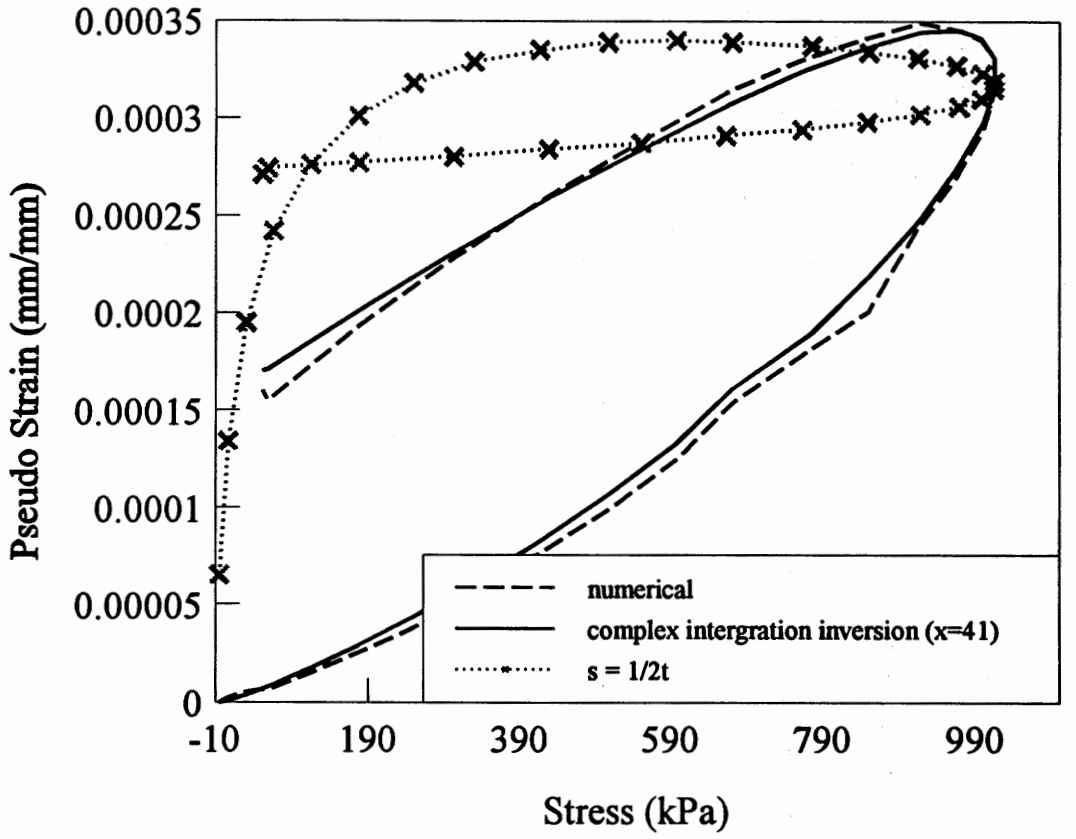

Figure 16. Comparison of Stress vs. Pseudo-Strain Curves for Sample M/DG/1.

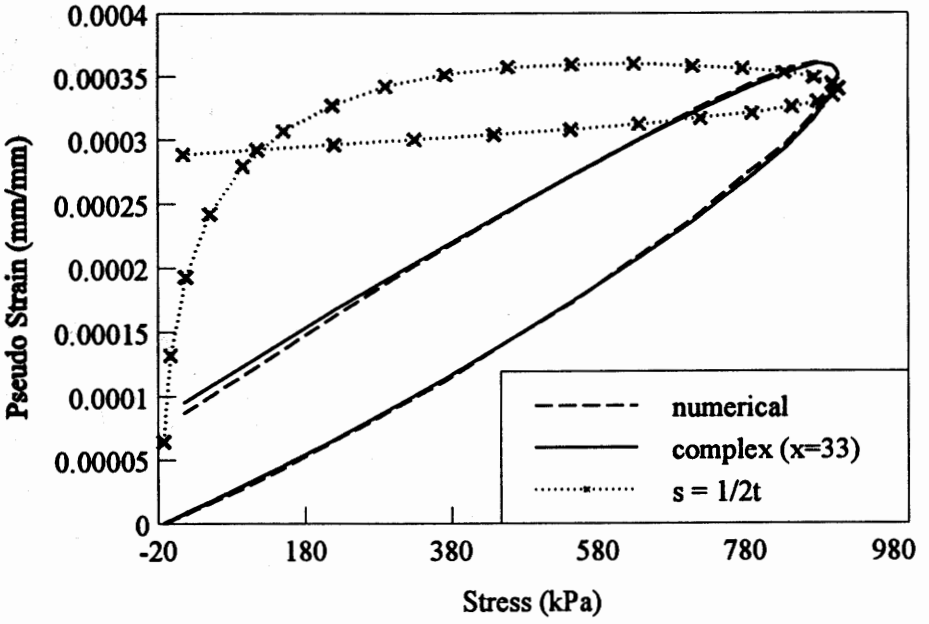

Figure 17. Comparison of Stress vs. Pseudo-Strain Curves for Sample M/DG/3.

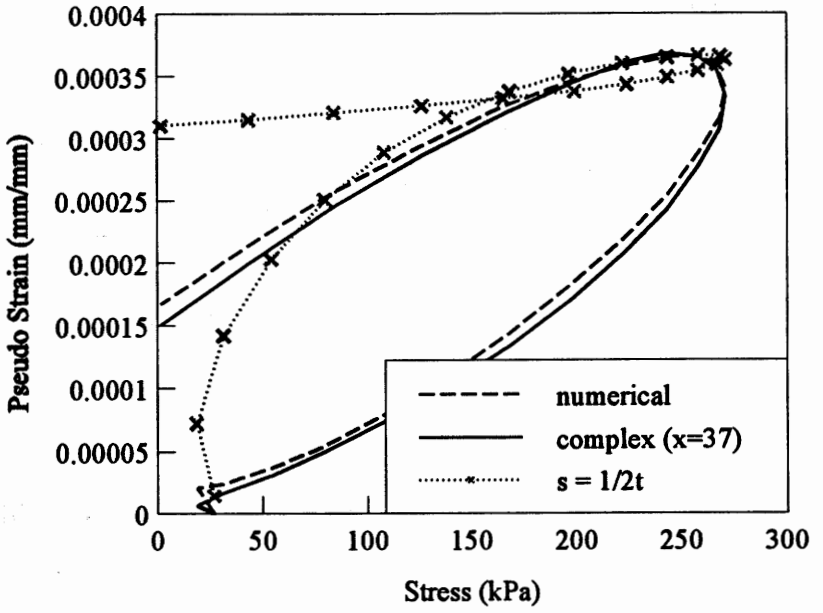

Figure 18. Comparison of Stress vs. Pseudo-Strain Curves for Sample D/DG/11.

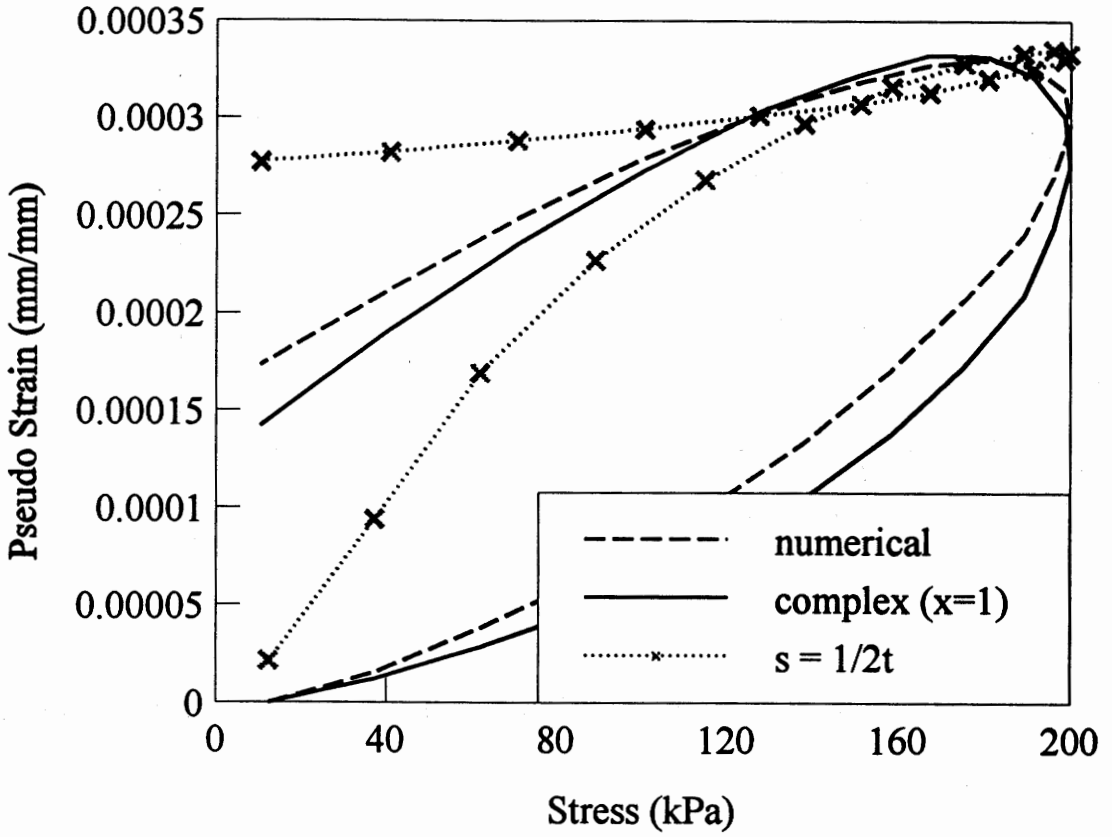

Figure 19. Comparison of Stress vs. Pseudo-Strain Curves for Sample D/DG/12.

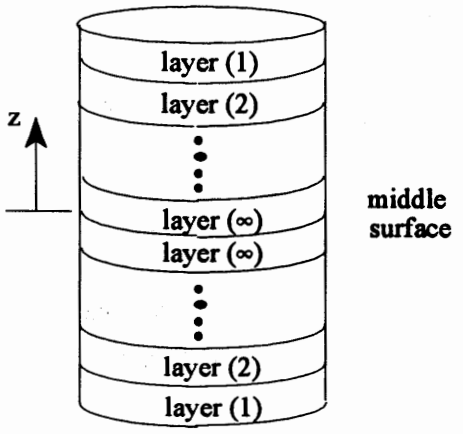

Figure 20. A Cylinder Specimen in a Series Mode.

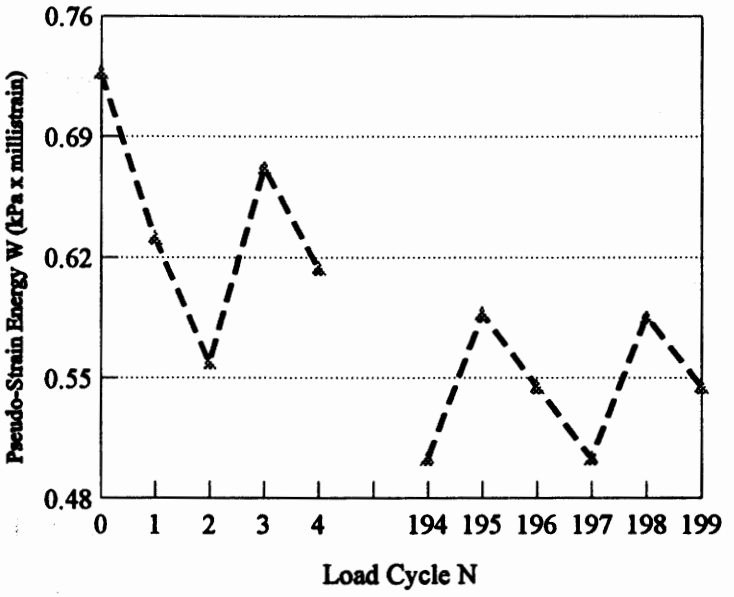

Figure 21. Pseudo-Strain Energy vs. Load Cycle for Sample B/DG/23 During Load Period 1.

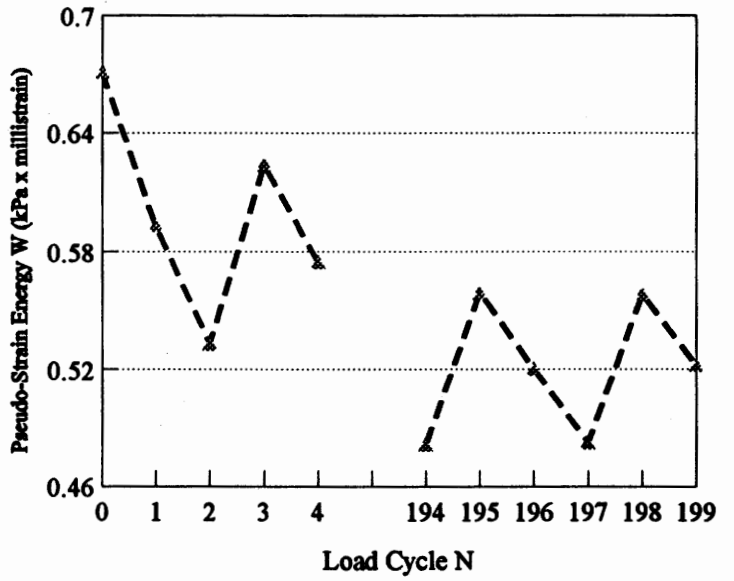

Figure 22. Pseudo-Strain Energy vs. Load Cycle for Sample B/DG/23 During Load Period 2

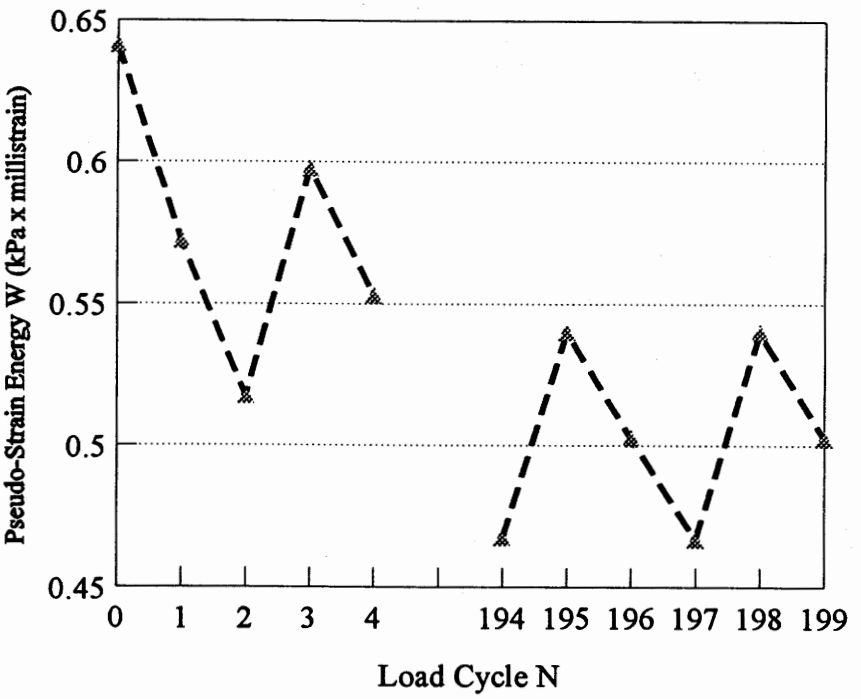

Figure 23. Pseudo-Strain Energy vs. Load Cycle for Sample B/DG/23 During Load Period 3.

CHAPTER 4: THE FINITE ELEMENT MODEL FOR MICROCRACK GROWTH

Various numerical techniques, such as finite difference, finite element, and boundary integral methods, have been applied to crack problems over the past two decades. Of these, the finite element method (FEM) has been used extensively. The task of this section is to apply continuum fracture mechanics (CFM) and derive a finite element formulation with which the fracture properties of asphalt mixes can be calculated. The first section outlines the finite element formulation for only one microcrack. By using the energy criterion and the CFM concept, a mechanical equation to describe the damage behavior was established. The formulation was further expanded for the cases of multiple microcracks. The Weibull distribution was then utilized to simulate microcrack growth with load repetition. Finally, the system identification (SID) method and fatigue data from the trapezoid strain loading tests were adapted in the microcrack analysis.

Finite Element Formulation for One Microcrack

Many FEM programs are available to analyze plane crack problems. The MICROCRACK code developed in this research is based on the work of Lytton et al.(1993) and the fracture program developed by Owen and Fawkes (1980) with two major modifications, which are the finite element matrixes for axially symmetric solids and the implementation of the finite element formulation. Because the axially symmetric FEM have been well documented, only the microcrack formulation is included in this section.

As shown in Figure 24(a), the finite element with microcrack length 2c is assumed to be isotropic. The elastic properties are the same in all directions. The Young's modulus and Poisson's ratio under stresses σ and τ are denoted by E and ν, respectively. Following the Griffith model (1920), the total energy per unit area U_c for the cracked element is given by:

$$U_c = \frac{[\sigma^2 + 2(1+\nu)\tau^2]}{2E}\left\{1 + 2\pi\left(\frac{c}{bl}\right)\left[\frac{4\Gamma E}{\pi[\sigma^2 + 2(1+\nu)\tau^2]} - c\right]\right\} \qquad (43)$$

where $G=E/2(1+\nu)$, Γ is the surface energy density, 2c is the microcrack length, and b and l are the width and height of the finite element, respectively.

To calculate the total energy stored in the fictitious undamaged body, the effective stiffness is introduced. Furthermore, the orientation of the microcrack is expected in the direction of the principal planes. The equivalent uncracked element is modeled as an orthotropic material. It is assumed that the modulus parallel to the orientation of the microcrack does not change with load repetitions, but the modulus perpendicular to the microcrack is reduced. The reduced modulus is obtained by equating the total energy associated with the cracked element to the total energy associated with the fictitious uncracked element.

The total energy per unit area U for the fictitious uncracked element is:

$$U = \frac{1}{2}(\sigma_r \epsilon_r + \sigma_z \epsilon_z + \sigma_\theta \epsilon_\theta + \tau_{rz} \gamma_{rz}) \tag{44}$$

and ϵ_r, ϵ_z, ϵ_θ and r_{rz} are given by:

$$\begin{Bmatrix} \epsilon_r \\ \epsilon_z \\ \epsilon_\theta \\ \gamma_{rz} \end{Bmatrix} = \begin{bmatrix} C_{11} & C_{12} & C_{13} & C_{14} \\ C_{21} & C_{22} & C_{23} & C_{24} \\ C_{31} & C_{32} & C_{33} & C_{34} \\ C_{41} & C_{42} & C_{43} & C_{44} \end{bmatrix} \begin{Bmatrix} \sigma_r \\ \sigma_z \\ \sigma_\theta \\ \tau_{rz} \end{Bmatrix} \tag{45}$$

where C_{ij} is the compliance component in the cylindrical coordinate system.

The matrix [C] is determined from the following transformation equation:

$$[C] = [T_\sigma]^T [C'][T_\sigma] \tag{46}$$

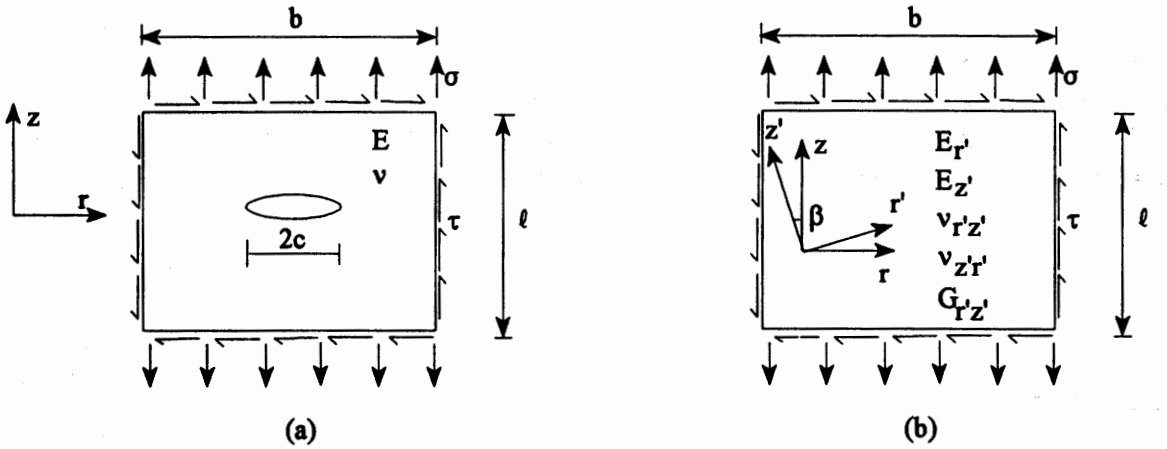

Figure 24. The Microcrack Model: (a) Isotropic Material for Damaged State, (b) Orthotropic Material for Fictitious Undamaged State.

where $[T_\sigma]$ is the transformation matrix and [C'] is the local compliance matrix in its principal coordinates, which is inclined at β radius with reference to the global r-z coordinate.

The $[T_\sigma]$ and [C'] matrices are defined as:

$$[T_\sigma] = \begin{bmatrix} \cos^2\beta & \sin^2\beta & 0 & 2\cos\beta\sin\beta \\ \sin^2\beta & \cos^2\beta & 0 & -2\cos\beta\sin\beta \\ 0 & 0 & 1 & 0 \\ -\cos\beta\sin\beta & \cos\beta\sin\beta & 0 & \cos^2\beta-\sin^2\beta \end{bmatrix} \tag{47}$$

$$[C'] = \begin{bmatrix} 1/E_{r'} & -\nu_{z'r'}/E_{z'} & -\nu_{\theta'r'}/E_{\theta'} & 0 \\ -\nu_{r'z'}/E_{r'} & 1/E_{z'} & -\nu_{\theta'z'}/E_{\theta'} & 0 \\ -\nu_{r'\theta'}/E_{r'} & -\nu_{z'\theta'}/E_{z'} & 1/E_{\theta'} & 0 \\ 0 & 0 & 0 & 1/G_{r'z'} \end{bmatrix} \tag{48}$$

where ν_{ij} characterizes the strain in the j direction due to the stress in the i direction.

According to energy concept (Maxwell-Betti reciprocal theorem), the local compliance [C'] is a symmetrical matrix. To further simplify Equation (44), the stress components σ_r and σ_θ are ignored. By substituting Equations (47) and (48) into Equation (45), the total energy U for the uncracked element can be written as:

$$U = \frac{1}{2}(C_{22}\sigma^2 + 2C_{24}\sigma\tau + C_{44}\tau^2) \tag{49}$$

where $\sigma = \sigma_z$, $\tau = \tau_{rz}$ and the components C_{22}, C_{24} and C_{44} are defined as follows:

$$C_{22} = \frac{1}{E_{r'}}[\sin^4\beta - 2\nu_{r'z'}\cos^2\beta\sin^2\beta] + \frac{\cos^4\beta}{E_{z'}} + \frac{\cos^2\beta\sin^2\beta}{G_{r'z'}} \tag{50}$$

$$C_{24} = \frac{\sin2\beta\sin^2\beta}{E_{r'}} - \frac{\nu_{r'z'}}{E_{r'}}\sin2\beta\cos2\beta - \frac{\sin2\beta\cos^2\beta}{E_{z'}} + \frac{\sin2\beta\cos2\beta}{2G_{r'z'}} \tag{51}$$

$$C_{44} = 4\cos^2\beta\sin\beta\frac{(1+2\nu_{r'z'})}{E_{r'}} + \frac{4\cos^2\beta\sin^2\beta}{E_{z'}} - \frac{(4\cos^4\beta\sin^2\beta-1)}{G_{r'z'}} \tag{52}$$

If the local coordinate system is set such that r' - axis is always parallel with the orientation of the microcrack, we can assume:

$$E_{r'} = E = \textit{original Young's modulus} \tag{53}$$

$$\upsilon_{r'z'} = \upsilon = \textit{original Poisson's ratio} \tag{54}$$

$$E_{z'} = E' = \textit{reduced Young's modulus} \tag{55}$$

$$G_{r'z'} = G' = \textit{reduced shear modulus} \tag{56}$$

The reduced Young's modulus E' is perpendicular to the orientation of the microcrack. The reduced shear modulus G', at a given load cycle, is related to E' through the following relationship:

$$G' = \frac{E'}{2(1+\nu)} \tag{57}$$

Substituting Equations (53) through (57) into Equations (50), (51), and (52) and solving for C_{22}, C_{24}, and C_{44}, Equation (51) becomes:

$$U = \frac{F_1+F_2}{2E'} + \frac{F_3}{2E} \tag{58}$$

where

$F_1=\sigma^2 \cos^4\beta-2\sigma\tau \sin2\beta \cos^2\beta + 4\tau^2 \cos^2\beta \sin^2\beta$
$F_2=2(1+\nu)\sigma^2 \cos^2\beta \sin^2\beta + 2(1+\nu)\sigma\tau \sin2\beta \cos2\beta -2\tau^2 (1+\nu) (4 \cos^2\beta \sin^2\beta -1)$
$F_3=\sigma^2(\sin^4\beta-2\nu\cos^2\beta\sin^2\beta)+2\sigma\tau\sin2\beta\sin^2\beta-2\sigma\tau\nu \sin2\beta\cos2\beta+4\tau^2(1+2\nu)\cos^2\beta\sin^2\beta$

By equating Equations (58) and (43), the reduced modulus E' is determined as:

$$E' = \frac{F_1 + F_2}{F_4 \left\{ 1 + 2\pi \frac{c}{bl} \left(\frac{4\Gamma E}{\pi F_4} - c \right) \right\} - F_3} E \tag{59}$$

where $F_4=\sigma^2+2(1+\nu)\tau^2$.

The length c is the internal state variable in this microcrack model. For a strain-controlled test, there is no sudden failure and E' gradually decreases with load repetitions. Therefore, the length c for modulus E'_{min} can be solved with nonlinear finite element programs.

Finite Element Formulation for Multiple Microcracks

If, instead of one microcrack, there are m microcracks existing in the finite element, the probability of having a microcrack length c_i is defined as:

$$\frac{m_i}{m} = p(c_i) \tag{60}$$

where m_i is the number of microcracks with length c_i.

Back to the energy equivalence, Equation (59) can be expressed either in the summation form:

$$E' = \frac{F_1 + F_2}{F_4 \left\{ 1 + 2\pi \frac{m}{bl} \sum_{i=1}^{k} p(c_i)\, c_i \left(\frac{4\Gamma E}{\pi F_4} - c_i \right) \right\} - F_3} E \tag{61}$$

or in the integral form:

$$E' = \frac{F_1 + F_2}{F_4 \left\{ 1 + 2\pi \frac{m}{bl} \int cp(c) \left(\frac{4\Gamma E}{\pi F_4} - c \right) dc \right\} - F_3} E \tag{62}$$

In Equations (61) and (62), the microcrack density m/bl is assumed to be a function of the maximum stress σ_{max} in the loading history. Specifically, the following model is used:

$$\left(\frac{m}{bl}\right) = d(\sigma_{max} - \sigma_o)^q \tag{63}$$

where

σ_o = a threshold stress below which no microcrack growth occurs, and
d, q = model coefficients.

The probability p(c) changes as microcracks grow. In this research, p(c) is assumed to follow a Weibull distribution function, which is illustrated in Figure 51. The function is given by:

$$p(c) = \lambda\gamma(\lambda c)^{\gamma-1} e^{-(\lambda c)^{\gamma}} \tag{64}$$

where the scale parameter λ and the shape parameter γ are further related to load repetitions according the following equations:

$$\gamma = p\, e^{-(\frac{r}{N})^{s}} \tag{65}$$

$$\lambda = a\, e^{-(\frac{f}{N})^{g}} \tag{66}$$

where N is the number of load cycles and p, r, s, a, f, and g are model coefficients.

Replace $(\lambda c)^{\gamma}$ with t in Equation (64) and noteing that

$$dc = \frac{1}{\lambda\gamma}\, t^{\frac{1}{\gamma}-1} \tag{67}$$

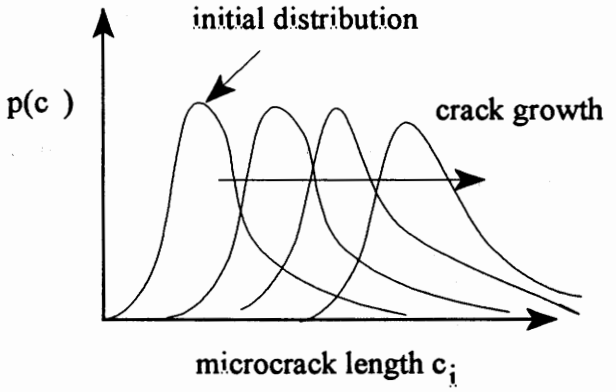

Figure 25. Weibull Distribution Function for Microcrack Length c_i.

The integral term in the denominator of Equation (62) can be evaluated from the following expressions:

$$\int cp(c)dc = \bar{c} = \frac{I\,[1+\ 1/\gamma\ ,\ (\lambda c_{max})^{\gamma}\ ] - I\,[1+\ 1/\gamma\ ,\ (\lambda c_0)^{\gamma}\ ]}{\lambda} \tag{68}$$

$$\int c^2 p(c)dc = \overline{c^2} = \frac{I\,[1+\,2/\gamma\ ,\ (\lambda c_{max})^{\gamma}\ ] - I\,[1+\,2/\gamma\ ,\ (\lambda c_0)^{\gamma}\ ]}{\lambda^2} \tag{69}$$

where

I = the Incomplete Gamma function with two parameters,
$\bar{c}$ = the mean microcrack length,
$\overline{c^2}$ = the mean of the squared microcrack length,
c_0 = the initial microcrack length, and
c_{max} = the maximum microcrack length.

Thus, Equation (62) can be rewritten as:

$$E' = \frac{F_1 + F_2}{F_4 \left\{ 1 + 2\pi \frac{m}{bl} \left(\frac{4\Gamma E}{\pi F_4}\,\bar{c} - \overline{c^2} \right) \right\} - F_3} E \tag{70}$$

The reduced modulus E' in Equation (70) can be further related to the rate of change of dissipated pseudo-strain energy. It is proposed that the same fracture properties that control the propagation of visible cracks control the propagation of microcracks. The change in dissipated pseudo-strain energy per load cycle dW/dN is given by:

$$\frac{\frac{dW}{dN}}{t\frac{d\bar{c}}{dN}} = J_I + J_{II} \tag{71}$$

Following Schapery's method, the rate of mean microcrack growth can be given by:

$$\frac{d\bar{c}}{dN} = A(K_I^2 + K_{II}^2)^{n/2} \tag{72}$$

where K_I^2 and K_{II}^2 are given by $\sigma^2\pi\bar{c}$ and $\tau^2\pi\bar{c}$, respectively.

By substituting Equation (72) into Equation (71) it can be shown that:

$$\frac{dW}{dN} = \frac{F_4}{E} At(\pi\bar{c})^{1+\frac{n}{2}} (\sigma^2 + \tau^2)^{\frac{n}{2}} \tag{73}$$

Therefore, the finite element formulation for multiple microcracks contains the original modulus E, the reduced modulus E', and the change in dissipated strain energy per load cycle dW/dN:

$$E' = \frac{F_1 + F_2}{F_4 \left\{ 1 + 2\pi \frac{m}{bl} \left[\frac{4\Gamma A t \pi^{\frac{n}{2}} (\sigma^2 + \tau^2)^{\frac{n}{2}}}{\frac{dW}{dN}} \overline{c}^{2+\frac{n}{2}} - \overline{c^2} \right] \right\} - F_3} E \tag{74}$$

The measured value of the dissipated pseudo-strain energy, $\frac{dW}{dN}$, as discussed earlier on pages 22-29, along with the measured reduced modulus, E′, are both inserted into equation (74) as they change with the number of load cycles, N. The multiple values permit the back-calculation of the microfracture properties A,n,p,d, and q. These properties are first introduced into equations (72), (72), (65), (63) and (63), respectively.

System Identification Method

With the formulation presented in Equation (74), fatigue data from trapezoidal strain loading tests were analyzed to back-calculate the fracture parameters. The objective of the System Identification method (SID) is to estimate system characteristics by using only input and output data from the system. The process is identified when the error between the model and the real process is minimized in some sense. Otherwise, the process must be modified until the desired level of agreement is achieved.

The SID scheme can be modeled with a mathematical representation. The dW/dN is taken as the output to be compared. Based on the Taylor Series expansion, the following linear equations are derived for adjusting the input parameters:

$$\{r\} = [F]\{\alpha\} \tag{75}$$

$$\{P\}^{k+1} = \{P\}^k (1 + \{\alpha\}) \tag{76}$$

where the vector {r} is the analysis difference between the model and the real system, the matrix [F] is the sensitivity matrix, and the vector $\{\alpha\}$ represents the parameter adjustments that can be generated numerically with the trial and error process. The element F_{ki} reflects the model output component f_k to the input parameter p_i. The parameter set {P} is updated each time with a new $\{\alpha\}$ until the difference vector {r} is acceptable. This SID algorithm is plotted in Figure 26.

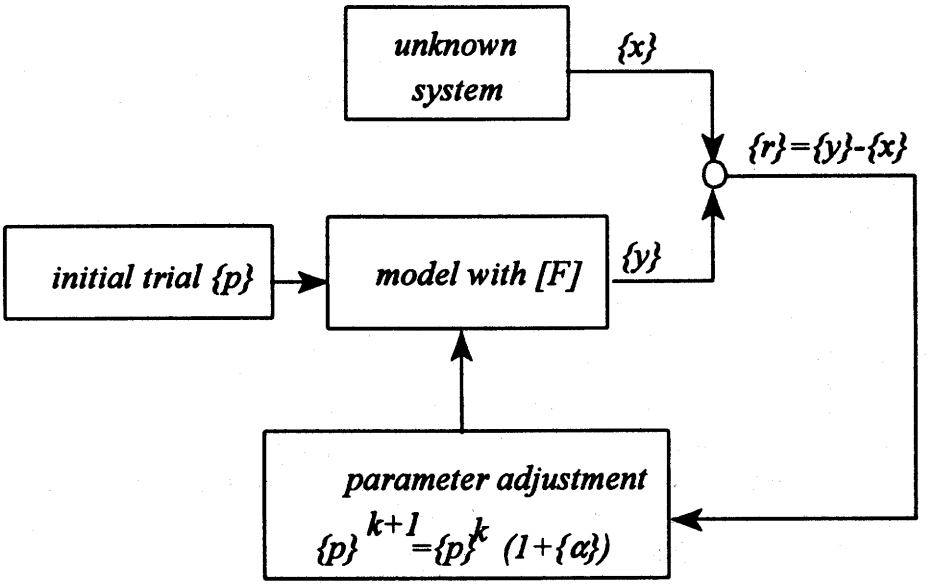

Figure 26. System Identification Diagram.

Microcrack Analysis

A sensitivity analysis of the model was initially conducted to identify the parameters that most significantly influence the predictions. It was found that the dW/dN is most sensitive to the following parameters:

1. the fracture coefficient A in Paris' law,
2. the fracture exponent n in Paris' law, and
3. the coefficient p for the microcrack distribution parameter γ.

From the fatigue test data, the pseudo-strain energy history is of a sawtooth form as discussed previously. The drop in the level of total pseudo-strain energy in the sample represents a loss of some of the cross-sectional area of the sample due to the opening up of a new crack area. This transfers the load carried by the sample to the remaining intact cross section of the sample, increasing the stress on that reduced area and increasing the pseudo strain in that area also. In this process the total pseudo-strain energy per unit volume in the sample remains the

same or very nearly the same. Thus, the trend in the pseudo-strain energy history after a drop in the level of total energy in the sample is the same as the trend in the pseudo-strain energy history before the drop. Because what is important in predicting the rates of fracture is the rate of change of the pseudo-strain energy, the curves representing the growth of curves representing the growth of microcracks with load repetitions were joined end-to-end for the purpose of analysis. A function that best fits the modified pseudo-strain energy was initially identified and used to calculate dW/dN. The task was performed by using the Jandel Scientific Table Curve. The sum of squares of error was calculated between the modified pseudo-strain energy and each function listed in the software. The function that resulted in the smallest sum of squares of error was chosen. This procedure yields the best fitting equation for all modified pseudo-strain energy as follows:

$$W = e^{a+bN^2} \tag{77}$$

The pseudo-strain energy for sample M/DG/25 during load period 1 is used here to illustrate the whole process. As illustrated in Figure 27, the energy at cycle 2 was escalated to the same level as one at cycle 1 and the modification was applied for energy values at cycles 7 and 16. In Figure 28, Equation (77) with a=-3.74245 and b=0.00089 was found to best fit the modified pseudo-strain energy with R^2=0.89.

A set of seed values for the fracture parameters is input to the MICROCRACK program. The SID method is used to adjust the input values. This iterative procedure is continued until the dW/dN predicted from the FEM best matches the dW/dN calculated from the fitted function. Two dW/dN curves are plotted in Figure 29. The back-calculated fracture parameters for selected specimens are shown in Tables 3 and 4. The mean microcrack lengths for trapezoidal strain-controlled tests are plotted in Figures 30 and 31.

Two approaches have been used to investigate microdamage healing: (1) calculation of a healing index based on the differences in dissipated strain energy before and after rest periods and (2) the use of fracture mechanics together with measurement of dissipated pseudo-strain energy as a means of investigating the rate of microcrack propagation as well as a change in the distribution of microcrack length upon loading and healing. The successful application of Schapery's fracture law and a microfracture and healing (MFH) method to the observed microcrack and macrocrack behavior of mix cylinder fatigue tests refines the understanding of fundamental fracture mechanics and will be discussed in the next section.

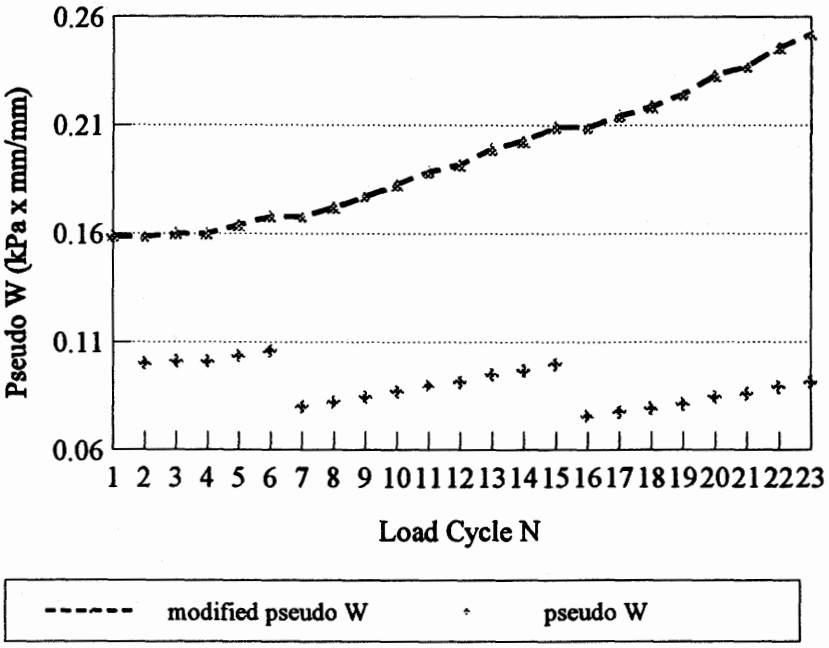

Figure 27. Modification of Pseudo-Strain Energy, W, for Sample M/DG/25 During Load Period 1.

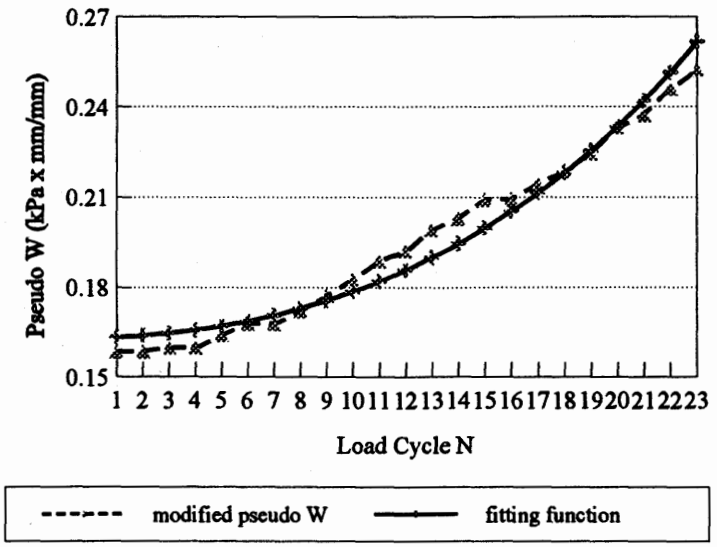

Figure 28. A Curve-Fitted Function $\exp(-3.74245+0.00089*N^2)$ for Modified Pseudo Energy W for Sample M/DG/25 During Load Period 1.

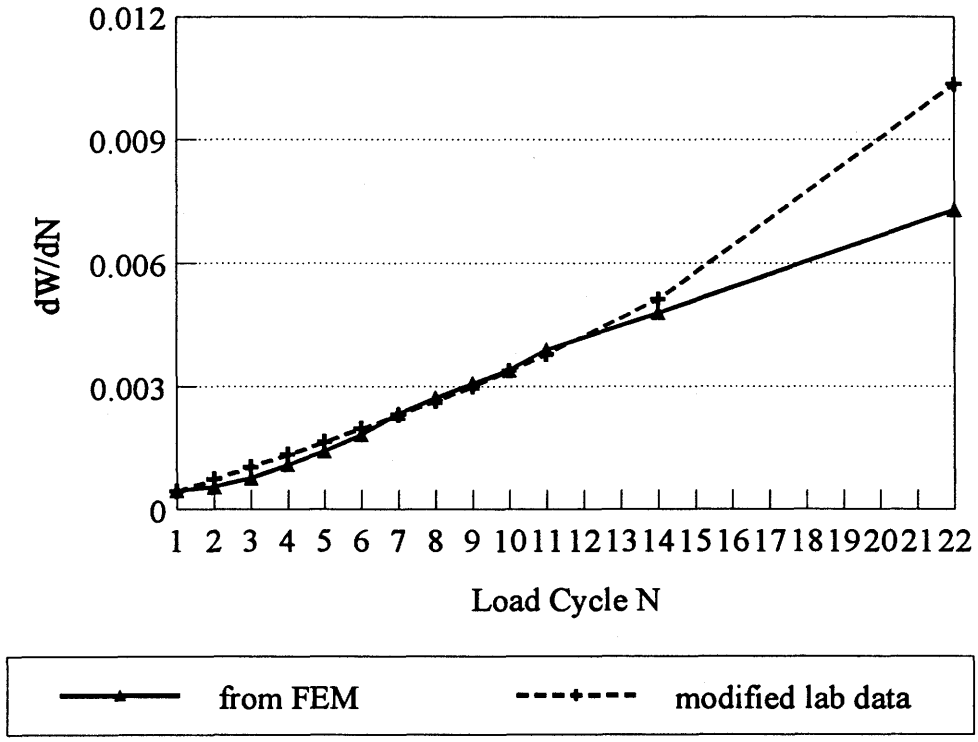

Figure 29. dW/dN from FEM and Modified Lab Data for Sample M/DG/25 During Load Period 1.

Table 3. Back-calculated Fracture Parameters from Trapezoidal Strain Data.

Sample	A	n	p
M/DG/19	0.000043	1.3	1.14
M/DG/25	0.000034	1.3	1.10
M/DG/21	0.000017	1.6	1.01
D/DG/17	0.000014	1.9	1.00
F/DG/4	0.000030	0.94	1.23
F/DG/6	0.000036	1.14	1.66
B/DG/4	0.000062	1.10	1.36
B/DG/3	0.000038	1.21	1.40
B/DG/5	0.000048	1.19	1.50
F/DG/2	0.000020	1.25	1.64
F/FG/3	0.000033	1.13	1.57
B/DG/2	0.000032	1.53	1.26

Table 4. Back-calculated Fracture Parameters from Haversine Strain Data.

Specimen	A	n	p
B/DG/23	0.000060	1.62	1.31
B/DG/25	0.000070	1.64	1.26
D/DG/38	0.000057	1.65	1.30
D/DG/43	0.000080	1.55	1.29
M/DG/40	0.000021	1.70	1.24
M/DG+P/7	0.000020	1.60	1.27
F/DG/19	.0000057	1.54	1.30
M/SMA/1	.0000085	1.58	1.23
M/SMA+L/10	0.000010	1.70	1.23
M/DG/46	0.000015	1.67	1.30
D/FG/61	0.000024	1.50	1.21
D/DG/9	0.000018	1.50	1.20

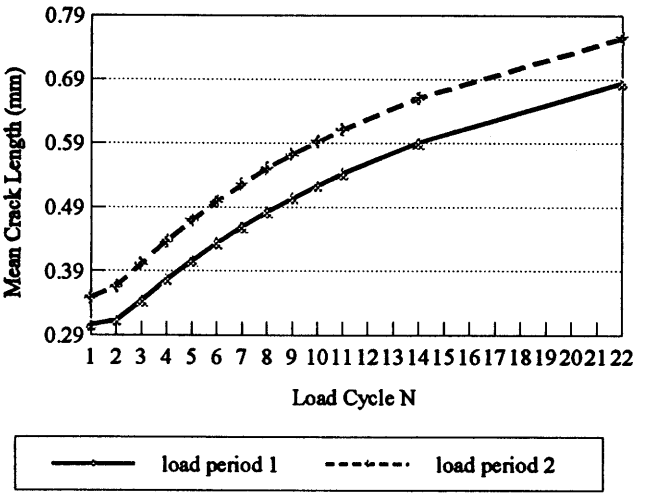

Figure 30. Mean Microcrack Length for Sample M/DG/21.

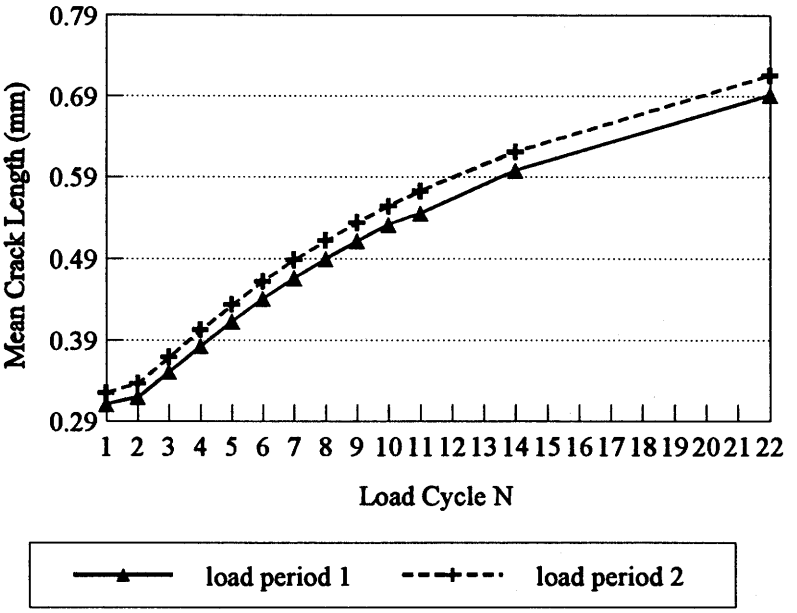

Figure 31. Mean Microcrack Length for Sample D/DG/17.

CHAPTER 5: FUNDAMENTAL LAWS OF THE RATES OF FRACTURE AND HEALING

Derivation of the Rate of Fracture Law

Schapery's fundamental law of fracture mechanics (1984) is stated as:

$$2\gamma_f = E_R \, D_f(t_\alpha) \, J_V \tag{78}$$

where

γ_f = the surface energy density of a crack surface (units: FL^{-1}).
E_R = an arbitrary constant with units of $F\,L^{-2}$. Its numerical value is commonly taken as 1.0 although in this report it is always taken as the maximum stress divided by the maximum pseudo strain. It makes Equation (78) dimensionally correct.
$D_f(t_\alpha)$ = the tensile creep compliance of a material corresponding to the time, t_α, that is required for a crack to move through the distance α, which is the length of the fracture process zone ahead of the crack tip (units: $F^{-1}\,L^2$).
J_V = the viscoelastic J-integral. This is the change of dissipated energy per unit of crack growth area from one tensile load cycle to the next (units: $F\,L^{-1}$).

Lytton proposed a corresponding fundamental law for material healing that is of the same form:

$$2\gamma_h = E_R \, D_h(t_\alpha) \, H_V \tag{79}$$

where

γ_h, E_R = the same meaning as before.
$D_h(t_\alpha)$ = the compressive creep compliance of a material corresponding to the time t_α, that is required for a crack to heal through the distance α, the length of the fracture process zone. Note that D_h is not necessary equal to D_f.
H_V = the viscoelastic H-integral. This is the change of dissipated pseudo-strain energy per unit of crack healing area from one compressive load cycle to the next.

The tensile and compressive compliances for asphalt-aggregate mixes can be expressed in a power law form as:

$$D_f(t) = D_{of} + D_{1f} \, t^{m_f} \tag{80}$$

$$D_h(t) = D_{oh} + D_{1h}\, t^{m_h} \tag{81}$$

and the times for the fracture and healing to traverse the length of the fracture process zone α are:

$$t_f = \frac{K_f\, \alpha}{\dot{f}} \tag{82}$$

$$t_h = \frac{K_h\, \alpha}{\dot{h}} \tag{83}$$

where

k_f, k_h = constants that depend upon the value of m. A common values of both are 1/3.
m_f, m_h = the slopes of log creep compliance versus log time curves for asphalt mixes.

The absolute crack speed $\dot{c}$ is the difference between the fracture speed $\dot{f}$ and the healing speed $\dot{h}$. Rearranging Equations (78) through (83) gives an expression for crack growth:

$$\dot{c} = \dot{f} - \dot{h}$$

$$= \frac{K_f \alpha (D_{1f}\, E_R\, J_V)^{\frac{1}{m_t}}}{(2\gamma_f - D_{of}\, E_R\, J_V)^{\frac{1}{m_t}}} - \frac{dh}{dt} \tag{84}$$

or

$$\frac{dc}{dN} = \int_o^{(\Delta t)_f} \frac{K_f \alpha (D_{1f}\, E_R\, J_V)^{\frac{1}{m_t}} dt}{(2\gamma_f - D_{of}\, E_R\, J_V)^{\frac{1}{m_t}}} - \frac{dh}{dN} \tag{85}$$

where

$(\Delta t)_f$ = the time permitted for fracture,
$(\Delta t)_h$ = the time permitted for healing, and
dt = $dN\,[\,(\Delta t)_f + (\Delta t)_h\,]$

In the course of analyzing the measured healing data, it was discovered that the actual rate of healing, $\frac{dh}{dt}$, is governed by two separate healing mechanisms, one of which is controlled by the non-polar ((Lifschitz-Van der Waals) and the other is controlled by the polar (Lewis acid-base) components of the surface energy densities, Γ_{LW} and Γ_{AB}, respectively. Both healing rates occur simultaneously and govern the actual healing rate according to the relation

$$\dot{h} = \dot{h}_2 + \left[\frac{\dot{h}_1 - \dot{h}_2}{1 + \frac{(\dot{h}_1 - \dot{h}_2)}{h_\beta}}\right](\Delta t)_h \tag{86}$$

where

$\dot{h}_1$, $\dot{h}_2$ = the healing rates generated by the non-polar ($\dot{h}_1$) and polar ($\dot{h}_2$) surface energies;

$\dot{h}_1$ = the actual healing rate;

$(\Delta t)_h$ = the rest period between load applications; and

h_β = a factor that varies between 0 and 1 and represents the maximum degree of healing that can be achieved by the asphalt binder.

A schematic graph of this relation is shown in Figure 32.

The theories explaining the two healing rates were developed by Lytton in this project ($\dot{h}_1$) and Schapery ($\dot{h}_2$) in (1989). The simpler forms of these two theoretical relations are given below in Equation (87) for ($\dot{h}_1$) and Equation (88) for ($\dot{h}_2$).

$$\dot{h}_1 = \left[\frac{K_h\, D_{1h}\, E_R\, H_v}{2\Gamma_{LW}}\right]^{\frac{1}{m_h}} \beta \tag{87}$$

and

$$\dot{h}_2 = \left[\frac{2\gamma_m E_R^2 D_{1h} \Gamma_{AB}}{(1-\nu^2) C_m^{\frac{1}{mh}} H_v}\right]^{\frac{1}{m_h}} \beta \tag{88}$$

The forms of these relations become more complicated when the glassy compressive compliance of the asphalt mixture, Δ_{oc}, is not zero. Because of their greater complexity, they will not be reported here.

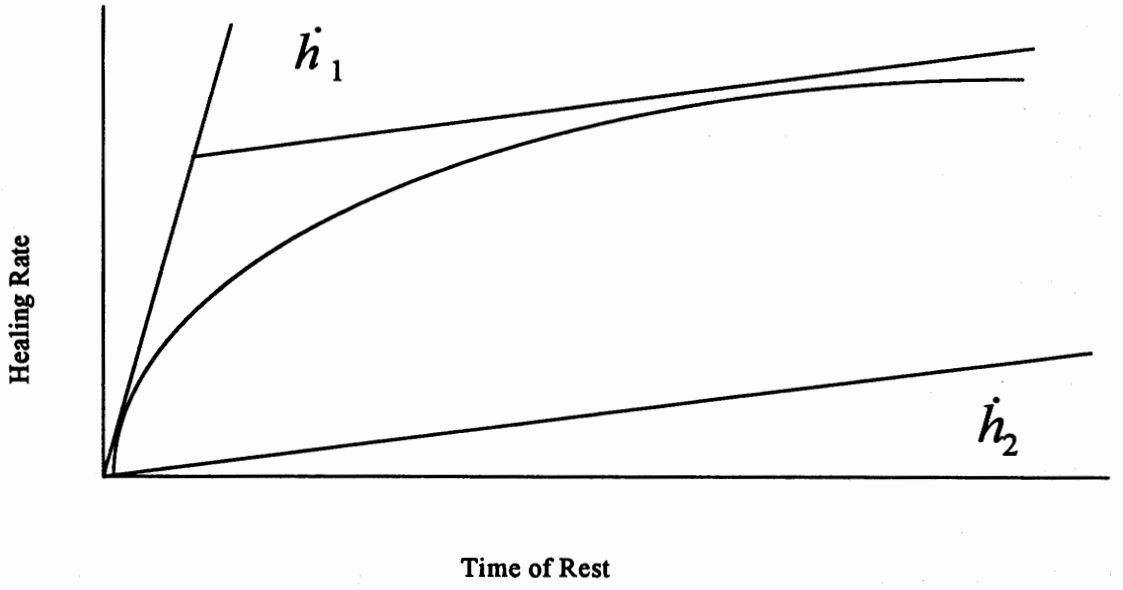

Figure 32. Schematic Graph of the Rate of Healing.

The variables not identified earlier are as follows:

β = length of the healing zone

ν = Poisson's ratio of the asphalt mixture

$$c_m = \frac{2m_h+1}{m_h+1} \tag{89}$$

$$\gamma_m = \left(\frac{\pi}{4}\right)^{\frac{1}{2}} \frac{\Gamma(1+m_h)}{\Gamma(1.5+m_h} \tag{90}$$

$\Gamma(\ )$ + the Gamma function of the argument in parentheses.

A striking difference between the two formulations is in the ratio of the surface energy Γ to the healing integral H_v. The early healing rate depends largely upon $\dot{h}_1$ which, in turn, depends upon H_v/Γ_{LW}. The long-term healing rate slows down to approach $\dot{h}_2$, which depends upon the ratio Γ_{AB}/H_v, the reciprocal of the healing rate governed by the non-polar surface energy.

The empirical evidence of these relations comes from the healing index, HI, measurements that were made and discussed in Volume 2. Although the healing index is a normalized, dimensionless number and is not the same as the actual length of the zone that is healed, it is still an indication of the rate at which healing proceeds. The rates of maximum and minimum change of healing index were determined by nonlinear regression analysis to be $\dot{h}_1$ and $\dot{h}_2$, as shown in Figures 33 and 34. The graph of $\dot{h}$, the early healing index rate and the non-polar (or LW component) surface energy component, Γ_{LW}, is shown in Figure 33. The graph of the $\dot{h}_2$, long-term healing rate and the polar (or AB component) surface energy component Γ_{AB}, is shown in Figure 34. The two relations reveal the inverse and direct relations predicted by Equations (87) and (88), respectively.

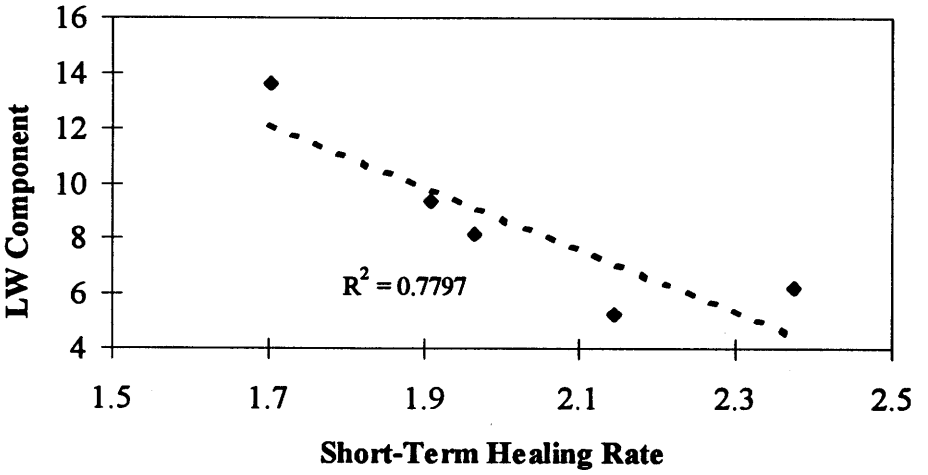

Figure 33. Relation Between the Early Healing Index Rate, $\dot{h}_1$, and the Non-Polar Surface Energy.

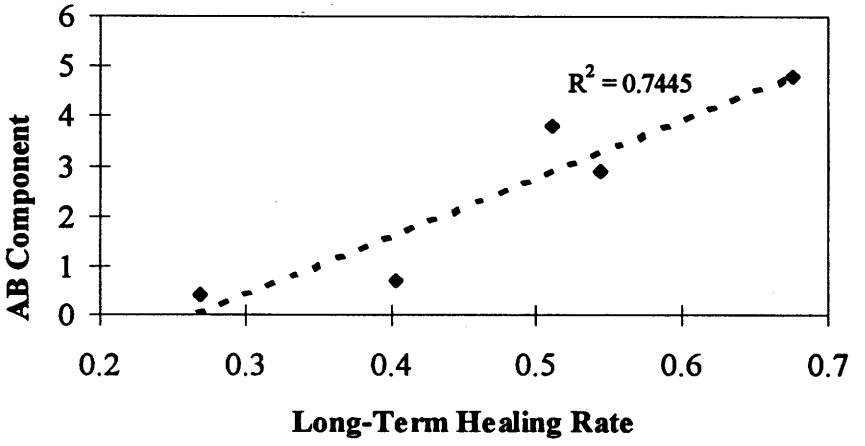

Figure 34. Relation Between the Long-Term Healing Index Rate , $\dot{h}_2$ and the Polar Surface Energy.

The rate of crack healing per load cycle, $\frac{dh}{dN}$, is given by an equation that is similar to equation (86), as shown below:

$$\frac{dh}{dN} = \dot{h}_2(\Delta t)_h + \frac{(\dot{h}_1 - \dot{h}_2)\,(\Delta t)_h}{1 + \frac{\dot{h}_1 - \dot{h}_2}{h_\beta}(\Delta t)_h} \tag{91}$$

The value of h_β was found empirically to depend upon the ratio of the surface energies, Γ_{AB}/Γ_{LW}, the polar divided by the non-polar component. Figure 35 shows this empirical relation which suggests that maximum healing may be achieved by an asphalt binder with a surface energy ratio less than 0.5. This is only part of the picture, however, since it is certain that h_β must also depend upon the compliance of the asphalt mix. All of the relations suggest a very productive line of further inquiry into the healing properties.

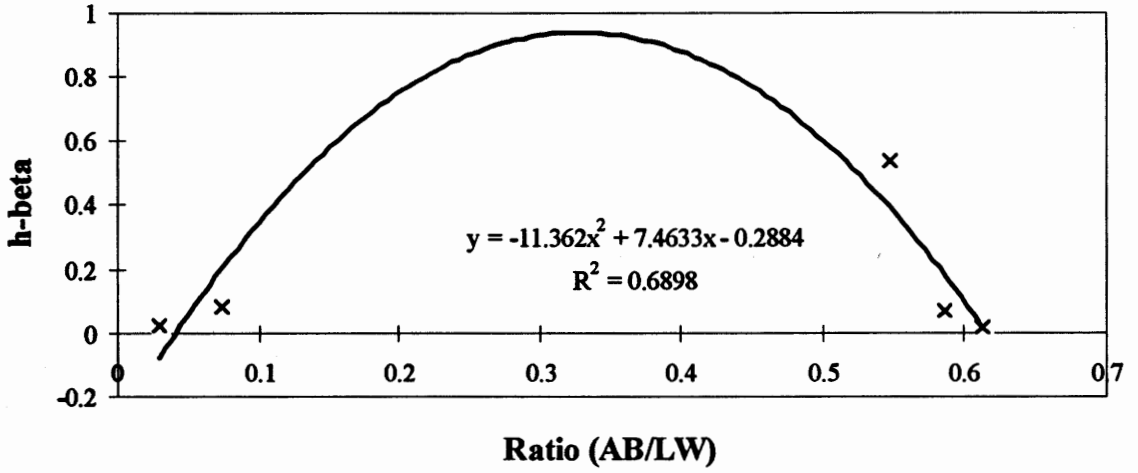

Figure 35. Empirical Relation Between h_β and the Ratio $\frac{\Gamma_{AB}}{\Gamma_{LW}}$.

Analysis of Load Test Data

The analysis of the laboratory test sample data was conducted assuming that healing is governed only by the total surface energy. All of the material properties that enter into the equations for fracture and healing were measured leaving only one unknown; the total surface energy, Γ. Having measured all the components of total surface energy separately, it was possible to compare this back-calculated value of Γ with the independently measured values. The two values compared very well, as is shown in Table 5 through 10 and discussed in the conclusions.

The form of the healing rate equation that was used in the analysis follows the early healing rate form, $\dot{h}_1$, of Equation (87) only for one principal reason. The rest interval between loads that was used in the test was too short for the long-term healing rate, $\dot{h}_2$, to have much influence.

The following section outlines the analysis that was done to arrive at the back-calculated laboratory values of the total surface energy Γ.

Following the same approach developed by Schapery (1973) for the stress intensity factor, the J_V and H_V integrals are defined according to the normalized wave form $w_f(t)$ and $w_h(t)$:

$$w_f(t) = \frac{J_V}{J_{V0}} \tag{92}$$

$$w_h(t) = \frac{H_V}{H_{V0}} \tag{93}$$

where J_{V0} and H_{V0} are the maximum values of J_V and H_V during loading time $(\Delta t)_f$ and $(\Delta t)_h$.

It is assumed that the growth or healing of microcracks in each load cycle is small and $w_f(t)$ and $w_h(t)$ have essentially the shapes of the difference of loading between two consecutive cycles. The size of fracture process zone α is estimated by the ratio of the J-integral to the area under the tensile strain curve of the material. An equation for this estimation is:

$$\alpha = \frac{J_V}{D_{1f}\,\sigma_f^2\,I_1} \tag{94}$$

where σ_f is the tensile strength of material, and I_1 is a number between 1 and 2.

Consider a special case that D_{of} and D_{oh} are much smaller than D_{1f} and D_{1h}. Substituting Equations (86), (87), and (88) to Equation (85) gives:

$$\frac{dc}{dN} = \left[\frac{k_f^{m_f} D_{1f} E_R}{2}\right]^{\frac{1}{m_f}} \int_0^{(\Delta t)_f} \frac{w_f(t)^{1+\frac{1}{m_f}}}{D_{1f} \Gamma_f^{\frac{1}{m_f}} \sigma_f^2 I_1} dt \, [J_{V0}]^{1+\frac{1}{m_f}} - \left[\frac{k_h^{m_h} D_{1h} E_R}{2}\right]^{\frac{1}{m_h}} \int_0^{(\Delta t)_h} \frac{w_f(t) w_h(t)^{\frac{1}{m_h}}}{D_{1h} \Gamma_h^{\frac{1}{m_h}} \sigma_h^2 I_1} dt \, [H_{V0}]^{\frac{1}{m_h}} [J_{V0}] \tag{95}$$

Schapery proposed two relationships between Paris' law parameter n and the material compliance property m:

$$n = \frac{2}{m} \qquad \textit{for strain controlled tests} \tag{96}$$

$$n = 2\left(1 + \frac{1}{m}\right) \qquad \textit{for stress controlled tests} \tag{97}$$

Experiments conducted by Lytton et al (1983) led to the following relationship for n:

$$n = 0.8 \left(1 + \frac{1}{m}\right) \tag{98}$$

To take into account the hyperelastic nature of the large strains in the fracture process zone, the parameter n_f for cohesive fracture may be written as:

$$n_f = r \left(1 + \frac{1}{m_f}\right) \tag{99}$$

and the coefficient r defines:

$$t_f = \left(\frac{K_f \alpha}{\dot{f}}\right)^{\frac{1}{r}} \tag{100}$$

$$\alpha = \left(\frac{J_V}{D_1 \sigma_f^2 I_1}\right)^r \tag{101}$$

The time t_f is a nonlinear function of fracture speed $\dot{f}$ and the fracture speed becomes:

$$\begin{aligned}\frac{df}{dN} &= \left[\frac{k_f^{\frac{m_f}{r}} D_{1f} E_R}{2}\right]^{\frac{r}{m_f}} \int_0^{(\Delta t)_f} \frac{w_f(t)^{r(1+\frac{1}{m_f})}}{D_{1f}^r \Gamma_f^{\frac{r}{m_f}} \sigma_f^{2r} I_1^r} dt \, [J_{V0}]^{r(1+\frac{1}{m_f})} \\ &= A_f [J_{V0}]^{n_f}\end{aligned} \tag{102}$$

The fracture surface energy density Γ_f can be determined from Equation (102):

$$\Gamma_f = \left[\frac{k_f^{\frac{m_f}{r}} D_{1f} E_R}{2}\right] \frac{\left[\int_0^{(\Delta t)_f} w_f(t)^{r(1+\frac{1}{m_f})} dt\right]^{\frac{m_f}{r}}}{D_{1f}^{m_f} A_f^{\frac{m_f}{r}} \sigma_f^{2m_f} I_1^{m_f}} \tag{103}$$

After studying asphalt properties and the parameter m_f back-calculated from the microcrack model, r is around 0.4. This value is smaller than Schapery's value based on a thin layer model and Lytton's value determined from thermal crack data. The curve fitting of dissipated pseudo-strain energy and the Γ_f back-calculation are according to the proposed reference modulus (E_R is a specific constant such that the maximum pseudo strain is equal to the maximum strain). To be consistent with Schapery's fundamental fracture theory (E_R is an arbitrary constant), Equation (103) is remodified as :

$$\Gamma_f = \left[\frac{k_f^{\frac{m_f}{0.4}} D_{1f} 1}{2}\right] \frac{\left[\int_0^{(\Delta t)_f} w_f(t)^{0.4(1+\frac{1}{m_f})} dt\right]^{\frac{m_f}{0.4}}}{D_{1f}^{m_f} (A_f \cdot E_R)^{\frac{m_f}{0.4}} \sigma_f^{2m_f} I_1^{m_f}} \tag{104}$$

The cohesive healing surface energy density Γ_h is proposed in a similar form:

$$\Gamma_h = \left[\frac{k_h^{\frac{m_h}{0.4}} D_{1h}\, 1}{2}\right] \frac{\left[\int_0^{(\Delta t)_h} w_f(t)^{0.4}\, w_h(t)^{\frac{0.4}{m_h}}\, dt\right]^{\frac{m_h}{0.4}}}{\left[\frac{\Gamma(1+m_h)\omega^{-m_h}}{\Gamma(1+m_f)\omega^{-m_f}}\right] D_{1h}^{m_h} (A_h \cdot E_R)^{\frac{m_h}{0.4}} \sigma_f^{2m_h} I_1^{m_h}} \tag{105}$$

where ω is the loading frequency and Γ is Gamma function.

Results Of Comparison

Equations (104) and (105) are valid when D_{of} is much smaller than D_{1f}. Mixes tested at room temperature are generally of this nature. If the tensile relaxation modulus for each specimen is represented in the pure power law, $D_f(t)$ can be determined from:

$$D_f(t)\, E_f(t) = \frac{\sin(m_f\, \pi)}{m_f\, \pi} \tag{106}$$

where $D_f(t) = D_{1f}\, t^{m_f}$.

The integral terms in Equations (104) and (105) are the area moment under the normalized waves $w_f(t)$ and $w_h(t)$ with orders related to material properties. The fracture and healing normalized waves for samples M/DG/19 and M/DG/25 are shown in Figures 36 and 37. The common values for k_f and k_h are 1/3 and I_1 is 1. The fracture Γ and healing Γ for mixes tested with trapezoidal strain loading are listed in Tables 5 and 6, respectively. The fracture Γ for mixes tested with haversine strain loading are listed in Table 7.

The fracture surface energy densities in Table 5 range between 135 and 518 mJ/m^2 for tests run at 25°C. The corresponding healing surface energy densities in Table 6 range between 100 and 417 mJ/m^2, always being smaller than the fracture surface energies. The two samples that were tested at 4°C, M/DG/1 and M/DG/25, showed a reversal of this trend, suggesting a different mode of fracture as will be discussed below.

Values of the fracture surface energies Γ_f taken from haversine strain loading tests range between 23 and 113 mJ/m^2 at a temperature of 22.2°C.

The values of Γ_f and Γ_h that are completely out of range are those that were calculated from the rate of change of dissipated pseudo-strain energy at a test temperature of 40°C. The numbers are in

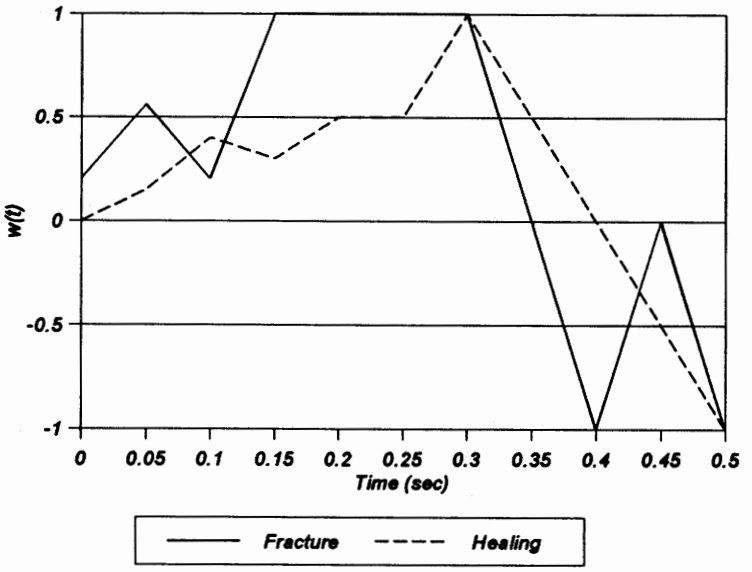

Figure 36. Normalized Wave Forms for Sample M/DG/19.

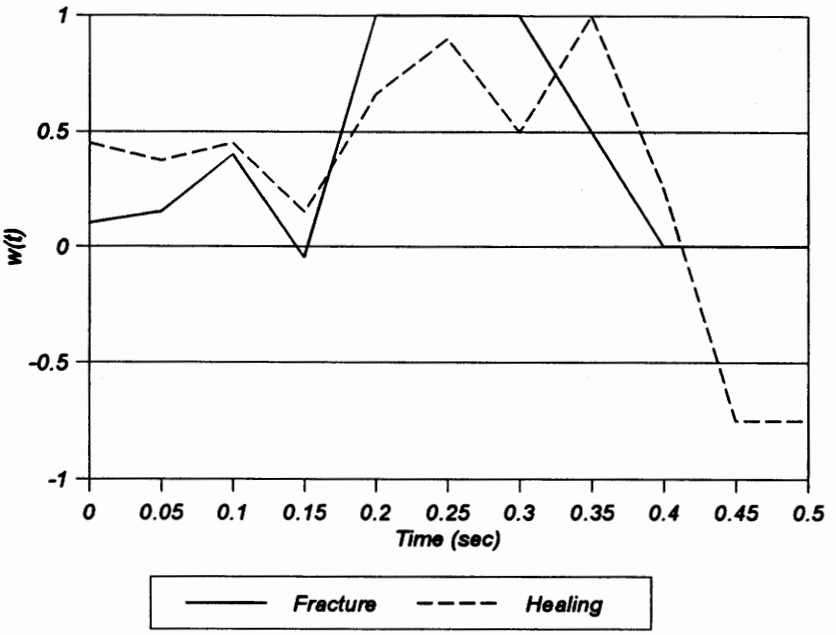

Figure 37. Normalized Wave Forms for Sample M/DG/25.

the thousands and are clearly out of range of the fracture and healing surface energies as measured independently, as discussed below. This strongly indicates that a damage process other than fracture, requiring much more energy than fracture, is at work at this elevated temperature. The most likely candidate is plastic flow.

The values of cohesive fracture and healing surface energies, Γ_f and Γ_h, as measured by the Wilhelmy Plate apparatus on different SHRP binders at 25°C are given in Table 8. This shows that the values are all within a narrow range: for fracture, between 27 and 32 mJ/m^2. These are taken from plunging an asphalt-coated plate into (wetting) and withdrawing it (dewetting) from a variety of fluids with known surface energies.

The values of adhesive fracture surface energies shown in Table 9 are calculated from the surface energies measured on binders by the Wilhelmy Plate apparatus and by the high vacuum adsorption Cahn Balance apparatus for the aggregates. The table shows the fracture surface energies for the work required to separate the aggregate surfaces from the various binders listed in the left-hand column. The aggregate was the Watsonville granite separated into the three size fractions shown in columns two through four. These numbers range between 174 and 223 mJ/m^2, showing the range within which adhesive fracture will occur.

Table 10 shows the corresponding calculated adhesive healing surface energies for the same sets of aggregate surfaces and asphalt binders. These range between 122 and 195 mJ/m^2, which are consistently lower than the fracture surface energies. These are calculated in the absence of water.

The difference in ranges of cohesive and adhesive fracture and healing surface energies measured by the independent means suggest that samples M/DG/19 and M/DG/25 in Table 5 and all but the last two 100-mm x 100-mm samples in Table 7 underwent cohesive fracture and healing. These ranges also suggest that all of the samples but the first four in Tables 5 and 6 underwent adhesive fracture and healing. The last two 100-mm x 100-mm samples in Table 7 have ranges of fracture surface energies in between the independently measured values of cohesive and adhesive fracture properties. This suggests that both processes were active in these two samples.

The systematic differences in the calculated surface energies of the 200-mm-high versus the 100-mm-high samples shows clearly the differences that are generated by a simple, tensile state of stress as opposed to a combined state that includes both tension and shear, which is induced by the proximity of the loading heads in the shorter samples. In the longer samples, all displacement measurements were made in the center third of the sample where the microcracks were adhesive and were formed and propagated by purely tensile stresses. On the other hand, in the shorter samples the microcracks were cohesive and were formed in the binder by a combination of tensile, shearing, and tearing mode stress intensity factors. The binder is apparently more susceptible to shearing microfracture initiation than to initiation by tensile stresses. However, once the microcracks open in the binder, evidence from our tests is that they continue to grow in the binder.

This consideration shows why it is important to choose the test sample geometry very carefully, taking into account not simply the modulus that can be inferred from the test but other material properties as well. This is particularly important when the modulus, Poisson's ratio, and the dominant fracture surface energy density and the fracture mode itself, adhesive or cohesive, all depend upon the stress state of the mix.

This is valuable information for selecting tests for specification values both for mix components and mixes themselves. The surface energy density tests with the Wilhelmy Plate on the binder and the high vacuum adsorption apparatus on the aggregates can be run separately and the surface chemistry formulas of Good and Van Oss (1992) can be used to compute the adhesive and cohesive surface energies both with and without the presence of water on the interface. Because the surface energies of asphalts do not vary much from one to another, there is no need for daily tests of this sort on refinery runs of asphalts. Also, aggregates can be screened separately by source, stratum, and pit by use of the adsorption apparatus. It is the aggregates that provide the greatest variability in adhesive surface energies.

Tests on mixes for fatigue resistance need to determine principally the tensile and compressive creep compliance information on the mix in different stress states. This can be done very conveniently by using frequency sweep tests on triaxial samples.

The important thing about all of this is that it is of paramount importance to get accurate measurements of the actual material properties as presented in this chapter. Sound and reliable specifications can be developed from them.

Table 5. Fracture Γ_f Analysis (Trapezoidal Strain Loading with 100-mm by 200-mm Samples).

Sample	D_{If}[1]	m_f	n_f	A_f	σ_f[2]	E_R[3]	Δt_f[4]	Γ_f[5]
M/DG/19[6]	1.59	0.46	1.31	0.000043	468	913587	0.5	29.8
M/DG/25[6]	2.32	0.54	1.30	0.000034	689	563321	0.5	26.0
M/DG/21[7]	19.72	0.63	1.21	0.000017	200	18106	0.5	7425.
D/DG/17[7]	19.72	0.62	1.27	0.000014	186	19099	0.5	9604.
F/DG/4[8]	14.79	0.72	0.96	0.000030	351	72631	0.5	392.3
F/DG/6[8]	8.12	0.49	1.14	0.000036	598	160101	0.5	135.4
B/DG/4[8]	35.09	0.54	1.10	0.000061	202	38308	0.5	303.9
B/DG/3[8]	20.88	0.43	1.21	0.000038	358	92186	0.5	517.8
B/DG/5[8]	19.72	0.46	1.19	0.000048	379	96150	0.5	299.7
F/DG/2[8]	11.89	0.57	1.25	0.000020	599	152476	0.5	275.4
F/FG/3[8]	13.20	0.53	1.13	0.000033	541	142864	0.5	211.5
B/DG/2[8]	245.6	0.62	1.53	0.000032	205	1944	0.5	157.5

[1]: D_{If} unit : 10^{-6} (1/kPa)
[2]: σ_t unit : kPa
[3]: E_R unit : kPa
[4]: Δt_f unit : second
[5]: Γ_f unit : mJ/m^2
[6]. Samples tested at 4°C
[7]: Samples tested at 40°C
[8]: Samples tested at 25°C

Table 6. Healing Γ_h Analysis (Trapezoidal Strain Loading with 100-mm by 200-mm Samples).

Specimen	D_{1h}[1]	m_h	n_h	A_h	σ_c[2]	E_R[3]	Δt_h[4]	Γ_h[5]
M/DG/19[6]	1.88	0.57	1.11	0.000011	-455	913587	0.5	57.2
M/DG/25[6]	2.46	0.59	1.25	0.000012	-634	563321	0.5	79.5
M/DG/21[7]	108.1	0.46	1.35	0.000019	-138	18106	0.5	32016
D/DG/17[7]	131.5	0.54	1.31	0.000023	-165	19099	0.5	23978
F/DG/4[8]	27.3	0.60	1.02	0.000017	-358	72631	0.5	192.3
F/DG/6[8]	19.7	0.56	1.10	0.000028	-558	160101	0.5	204.9
B/DG/3[8]	28.4	0.51	1.18	0.000043	-289	92186	0.5	417.1
B/DG/5[8]	26.9	0.53	1.10	0.000035	-317	96150	0.5	374.8
B/DG/2[8]	13.5	0.61	1.13	0.000036	-579	152476	0.5	100.5
F/DG/3[8]	17.4	0.60	1.15	0.000039	-489	142864	0.5	127.4

[1]: D_{1h} unit : 10^{-6} (1/kPa)
[2]: σ_c unit : kPa
[3]: E_R unit : kPa
[4]: Δt_h unit : second
[5]: Γ_h unit : mJ/m^2
[6]: Samples tested at 4°C.
[7]: Samples tested at 40°C.
[8]: Samples tested at 25°C

Table 7. Fracture Γ_f Analysis (Haversine Strain Loading with 100-mm x 100-mm Samples Tested at 22.2°C).

Specimen	D_{1f}[1]	m_f	n_f	A_f	σ_f[2]	E_R[3]	Δt_f[4]	Γ_f[5]
B/DG/23	0.038	0.338	1.62	0.000060	579	562797	0.13	27.2
B/DG/25	0.043	0.357	1.64	0.000070	482	518393	0.13	23.1
D/DG/38	0.039	0.329	1.65	0.000057	544	531294	0.13	32.6
D/DG/43	0.051	0.375	1.55	0.000080	482	445996	0.13	23.1
M/DG/40	0.027	0.380	1.70	0.000021	703	841596	0.13	23.1
M/DG+P/7	0.019	0.316	1.60	0.000020	737	1019646	0.13	29.9
F/DG/19	0.017	0.354	1.54	.0000057	1006	1279995	0.13	34.0
M/SMA/1	0.023	0.338	1.58	.0000085	779	1021798	0.13	38.1
M/SMA+L/10	0.021	0.350	1.70	0.000010	813	1216995	0.13	37.2
M/DG/46	0.025	0.358	1.67	0.000015	751	986895	0.13	25.8
D/FG/61	0.077	0.359	1.50	0.000024	372	312902	0.13	106.2
D/DG/9	0.078	0.305	1.50	0.000018	393	277399	0.13	113.1

[1]: D_{1f} unit : 10^{-6} (1/kPa)
[2]: σ_t unit : kPa
[3]: E_R unit : kPa
[4]: Δt_f unit : second
[5]: Γ_f unit : mJ/m^2

Table 8. Surface Energy Γ Calculated from Dewetting and Wetting Process.

Binder Type	Γ_r (mJ/m^2)	Γ_h (mJ/m^2)
AAA		11.85
AAB	32.47	
AAD	30.28	13.99
AAF	27.59	9.98
AAG		12.99
AAK	27.38	8.20
AAM		8.20

Table 9. Receding (Fractures) Surface Energies (Data from Gerry Elphingstone [1997] and Wenduan Li [1997]).

	Work (mJ/m^2)		
Material	SHRP#16-30	SHRP#30-50	SHRP < 74/um
AAB-1	214.0	216.7	218.9
AAD-1	177.6	179.4	183.7
AAF-1	174.9	177.2	179.5
AAF3	188.1	190.3	193.3
AAFa-	198.1	200.7	202.7
AAFTo	200.6	203.4	205.1
AAK-1	184.2	186.2	189.5
FI10	193.7	195.9	198.6
FI10a	223.4	226.5	227.6
JG34a	213.4	215.4	220.9
JG34T	210.7	212.8	217.9

Table 10. Advancing (Healing) Surface Energies (Data from Gerry Elphingstone [1997] and Wenduan Li [1997]).

Material	Work (mJ/m^2)		
	SHRP#16-30	**SHRP#30-50**	**SHRP < 74/um**
AAB-1	163.2	165.4	167.8
AAD-1	122.5	123.7	126.9
AAF-1	172.6	175.1	176.5
AAF3	150.3	151.9	155.4
AAFa-	175.2	177.6	179.7
AAFTo	169.4	171.9	173.9
AAK-1	166.3	168.8	170.0
FI10	161.6	163.6	166.3
FI10a	160.7	162.4	166.6
JG34a	191.0	193.7	195.1
JG34T	158.9	160.7	164.3

CONCLUSIONS

A finite element model of microcrack growth was developed that can successfully track microcrack damage and microcrack healing in uniaxial tensile, controlled-strain fatigue tests. The model is based on the Griffith model of total energy per unit area for a crack element. Damage due to microcrack growth causes a reduction in the stiffness of an element, which can be calculated through a mechanics-based relationship between energy and stiffness. The model was modified to accommodate a certain density of microcrack sizes based on a Weibull density function. The distribution of sizes and growth rate of the microcracks is also accounted for in the model.

Successful use of the model to track microcrack growth shows that the same basic fracture laws that control macrocrack growth also control microcrack growth. The microdamage model is able to accurately track the change in dissipated pseudo-strain energy throughout a uniaxial direct tensile fatigue test. Employing the relationship between the change in dissipated pseudo-strain energy and average crack length, crack growth can be tracked in a fatigue sample based on the history of the change of dissipated pseudo-strain energy throughout the test. The usefulness of this analytical tool to evaluate the effects of rest periods was proven as the recovery in dissipated pseudo-strain energy following rest periods was used to calculate the reduction in microcrack size distribution.

The finite element model based on fracture mechanics principles together with dissipated pseudo-strain energy recorded during uniaxial direct tensile, controlled-strain fatigue testing was used to "back-calculate" basic fracture properties of the various mixtures. These fracture properties were in turn used to "back-calculate" mixture surface energies using a fundamental law of viscoelastic fracture derived in this chapter. The calculated surface energies for the mixtures evaluated are within reasonable ranges when compared with measured surface energies for the various binders and aggregates used in the tests. Furthermore, the "backcalculated" surface energies for the various mixtures analyzed match the measured surface energies for the binders associated with the mixture.

REFERENCES

Alfrey, T., (1944) "Non-Homogeneous Stresses in Visco-Elastic Media". *Quarterly of Applied Mathematics*, Vol. 2, pp. 113-119.

Chen, C. W., (1997) "Mechanistic Approach to the Evaluation of Microdamage in Asphalt Mixes," Ph.D. Dissertation, Civil Engineering, Texas A&M University, Expected August 1997.

Elphingstone, G. M., (1977) "Adhesion and Cohesion in Asphalt-Aggregate Stiffness," Ph.D. Dissertation, Texas A&M University.

Li, W., (1977) "Evaluation of the Surface Energy of Aggregate Using the Cahn Balance," Texas A&M University, Chemical Engineering Department.

Good, R. J., and Van Oss, C. J., (1992) "The Modern Theory of contact Angles and the Hydrogen Bond Components of Surface Energies," Modern Approaches to Wettability, M.E. Schrader and G. Loeb, eds. *Plenum Press*, New York.

Griffith, A. A.,(1920) "The Phenomena of Rupture and Flow in Solids," *Philosophical Transactions, Series A*, Vol. 221, pp. 163-198.

Lytton, R. L., (1994) Personal Notes of R. L. Lytton.

Lytton, R. L., Shanmugham, U., and Garret, B. D., (1983) "Design of Asphalt Pavements for Thermal Fatigue Cracking," *Report FHWA/TX-83-284-4*, Texas Transportation Institute, Texas A&M University, College Station.

Lytton, R. L., Uzan, J., Fernando, E. G., Roque, R., Hiltunen, D., and Stoffels, S. M., (1993) "Development and Validation of Performance Prediction Model and Specifications for Asphalt Binders and Paving Mixes," *Report SHRP-A-357*.

Marek, R. and Herrin, M., (1968) "Tensile Behavior and Fatigue Characteristics of Asphalt Cements in the Thin Films," *Proceedings of the Association of Asphalt Paving Technologists*, Vol. 37, pp. 386-421.

Owen, D. R. J. and Fawkes, A. J., (1980) "Engineering Fracture Mechanics: Numerical Methods and Applications," *Pineridge Press Limited*, Swansea, U.K.

Schapery, R. A., (1984) "Correspondence Principles and Generalized J Integral for Large Deformation and Fracture Analysis of Viscoelastic Media," *International Journal of Fracture*, Vol. 25, pp. 195-223.

Schapery, R. A., (1973) "A Theory of Crack Growth in Visco-Elastic Media," Report MM 2764-73-1, *Mechanics and Materials Research Center*, Texas A&M University.

Schapery, R.A., (1989) "On the Mechanics of Crack Closing and Bonding in Linear Viscoelastic Media," *International Journal of Fracture*, Vol. 39, pp. 163-189.

Wylie, C. R. and Barrett, L. C., (1976) *Advanced Engineering Mathematics*, McGraw-Hill.